The Thesis committee for Peter Burrows Stetson

Certifies that this is the approved version of the following thesis:

# PIV Measurements of Flow-field Downstream of a Cylinder with and without Fairing and Comparison with CFD

APPROVED BY

SUPERVISING COMMITTEE:

Spyridon A. Kinnas, Supervisor

David G. Bogard

# PIV Measurements of Flow-field Downstream of a Cylinder with and without Fairing and Comparison with CFD

**by**

**Peter Burrows Stetson, B.A., M.S.**

**THESIS**

Presented to the Faculty of the Graduate School of

The University of Texas at Austin

in Partial Fulfillment

of the Requirements

for the Degree of

**MASTER OF SCIENCE IN ENGINEERING**

THE UNIVERSITY OF TEXAS AT AUSTIN

May 2013

Dedicated to my family for their enduring support, especially my grandmother, Bebe Stetson, my father, John, and my wife, Shannon.

# Acknowledgments

I wish to thank the people who helped make this work possible: my advisor, Dr. Kinnas, the members of the Ocean Engineering Group, especially Ye Tian, Xianming Yu, Liwei Han, and Chan-Hoo Jeon. I would also like to thank Tyler Megehe for his help fabricating the cylinder and fairing and Dr. Bogard for his thoughts and suggestions as the second reader.

# PIV Measurements of Flow-field Downstream of a Cylinder with and without Fairing and Comparison with CFD

Peter Burrows Stetson, M.S.E.
The University of Texas at Austin, 2013

Supervisor: Spyridon A. Kinnas

This work examines the ability of two-dimensional CFD models to predict the unsteady flow downstream of a cylinder, with and without fairing, in uniform flow. PIV measurements of the flow-field downstream of the cylinder and fairing in uniform flow are first presented. Slices of the flow at several locations along the cylinder are compared to show the variation of the flow in the cross-stream direction. Then the PIV flow is compared with RANS and LES simulations of the flow. Velocity time histories are compared and hydrodynamic coefficients are discussed. In a general sense, two-dimensional CFD can give a functional approximation of the unsteady flow field downstream of the cylinder or fairing.

# Table of Contents

# List of Tables

# List of Figures

# Chapter 1

# Introduction and Literature Review

## 1.1 Introduction

Turbulent flow past a cylinder is a complicated and well-studied phenomenon within fluid mechanics. Flow past a cylinder is especially interesting when the natural frequency of the cylinder matches the frequency of the vortices shed in the lee of the cylinder. When these frequencies approach each other, vortex-induced vibrations (VIV) occur and can lead to fatigue-driven failure. Modeling VIV is not a trivial task, and there is a large (and growing) amount of literature addressing the problem of VIV prediction (see [25] and [32] for excellent literature reviews of VIV).

Whether the cylinder is a marine riser or a cooling tube in a nuclear power plant, unexpected failure of such cylinders can have a catastrophic impact. While few (if any) examples of riser failure due to VIV exist in the literature, VIV is still regularly considered when designing marine risers [28]. Due to the large aspect ratios of deepwater marine risers and the high Reynolds numbers to which they are exposed, O(Re) =10e4 –10e6, computational fluid dynamics (CFD) can be a cost effective alternative to towed-tank experiments when studying VIV in risers [14].

While several authors [8, 26, 23] suggest that two-dimensional flow will not accurately capture the turbulence in shed vortices, others [1] support the notion that two-dimensional CFD could be accurate enough to predict hydrodynamic variables such as the coefficients of lift and drag. Two-dimensional CFD is faster and less computationally demanding than three-dimensional CFD. If hydrodynamic coefficients could be predicted with sufficient accuracy by two-dimensional CFD, this could prove advantageous in the design of tubulars subjected to VIV, such as marine risers.

In an effort to understand the ability of two-dimensional CFD to predict VIV we examine the efficacy of two-dimensional CFD in replicating flow-fields downstream of a cylinder, with and without fairing, as measured by PIV. This thesis builds upon work which examined unsteady flow around a cylinder subjected to waves [18] and is part of a larger project of which the ultimate goal is accurately modeling VIV. This thesis represents an early step in the project, where PIV and CFD velocity profiles, vorticity, and eventually forces on a fixed cylinder are compared in order to build confidence in how CFD predicts these variables on a fixed cylinder before moving to a fluid-structure interaction problem.

## 1.2 Literature Review of Vortex-induced Vibration Suppression in Marine Tubulars

Generally speaking, current solutions to VIV suppression fall into two categories: 1) surface protrusions that disrupt the correlation between the

shed vortices, thereby reducing the magnitude of oscillating forces (e.g. helical strakes) and 2) nearwake stabilizers that delay separation and shedding (e.g. fairings or splitter plates). For offshore drilling rigs, not only is VIV an issue for the marine riser, but if there is sufficient hydrodynamic drag on the riser, bending can be severe enough to halt operations [4]. As such, nearwake stabilizers tend to be a preferred VIV suppression method in deepwater drilling operations as they generally have reduced drag as compared to surface protrusion solutions. The focus of this review will be work dealing with VIV suppression for offshore drilling rigs, where drag is a concern. Surface protrusion methods will be addressed as well.

### 1.2.1 VIV and VIV Suppression

In the now declassified report by Grimminger [17], we find the beginnings of VIV suppression research. Grimminger and the United States Navy were interested in reducing VIV in submarine periscopes. Their work involved dragging an elastic cylinder through a wave basin (David Taylor Model Basin) with a towing mechanism. Using a towed tank for VIV-suppression testing is still common today and will be discussed subsequently. Grimminger's solution to reduce VIV in submarine periscopes was to attach rigid guide vanes to the cylinder (see figure 1.1 for the schematic of the vanes from the original paper). Grimminger found that the shape of the vane was unimportant insofar as VIV suppression, however differences in vane shape significantly affected drag [17].

Due to the high aspect ratio of deepwater risers (e.g D=2 ft, L=10e3

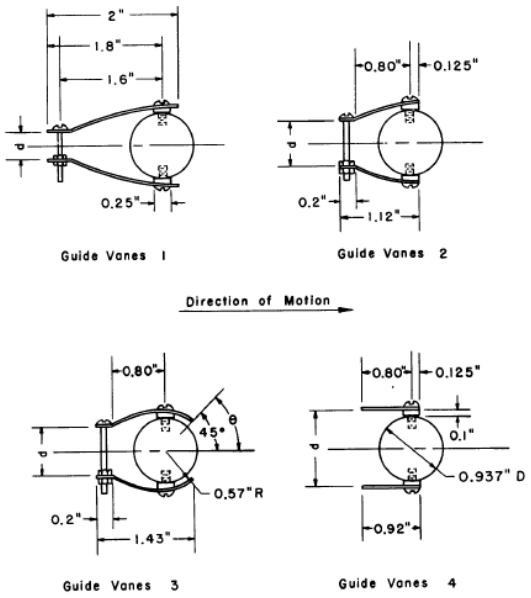


Figure 1.1: Schematic of rigid guide vanes for VIV suppression from the declassified Grimminger report [17]

ft $\rightarrow$ L/D=5e3), it is not always feasible to create a towed tank study for testing the efficacy of VIV suppression devices. Therefore modeling VIV is an important task whether it be via empirical models or CFD.

While the work following this review focuses on the fluids problem, VIV is inherently a fluid-structure-interaction problem. Therefore we will briefly address the basics of the structural side.The equation of motion generally used to describe the VIV of a cylinder oscillating normal to the flow is:

$$m\ddot{y} + c\dot{y} + ky = F \tag{1.1}$$

where $m$ is the structural mass, $c$ is the structural damping, $k$ is the spring con-

stant, $F$ is the fluid force in the transverse direction, and $y$ is a displacement. Often, the fluid force is approximated by:

$$F(t) = F_o \sin(\omega t + \phi) \tag{1.2}$$

which gives a response of

$$y(t) = y_o \sin(\omega t) \tag{1.3}$$

where $\phi$ is the phase angle, $t$ is time, $\omega = 2\pi f$, and $f$ is the frequency of oscillation of the cylinder. $F_o$ and $y_o$ are the initial force and initial transverse displacements, respectively. Khalak and Williamson [21] describe the response amplitude (a parameter of great interest in riser design) in terms of a set of non-dimensional parameters:

$$A^* = \frac{1}{4\pi^3} \frac{C_Y \sin\phi}{(m* + C_A)\zeta} \left(\frac{U^*}{f^*}\right)^2 f^* \tag{1.4}$$

where

$$f^* = \sqrt{\frac{m^* + C_A}{m^* + C_{EA}}} \tag{1.5}$$

$A^*$ is the non-dimensional amplitude of the cylinder displacement normal to the flow, $m^*$ is the non-dimensional added mass, $\zeta$ is the coefficient of damping, $U^*$ is the non-dimensional flow velocity, $C_A$ is the potential added mass coefficient and $C_{EA}$ is the "effective" added mass coefficient (which takes into account the apparent effect due to the total transverse fluid force in phase with the body acceleration, $C_Y * \cos\phi$). The effective added mass coefficient:

$$C_{EA} = \frac{1}{2\pi^3} \frac{C_Y \cos\phi}{A^*} \left(\frac{U^{*\,2}}{f^*}\right) \tag{1.6}$$

Equation 1.2.1 which describes the relative amplitude of the displacements in a given flow, is the equation of interest. With $A^*$(which is generally the dimensional amplitude normalized to the cylinder diameter and thus made non-dimensional), one can determine whether or not VIV will shut down operations, e.g. from excessive bending or the increased likelihood of fatigue driven failure in a marine riser, or perhaps the possibility of hitting nearby tubulars (relevant to both marine risers and cooling tubes in nuclear power plants). It is worth mention that equation 1.2.1 describes a scenario with only one degree of freedom (DOF). As pointed out by Jauvtis and Williamson [20], the freedom to oscillate in the in-line direction does affect the transverse vibration, especially at low mass ratios (i.e. $m^*<6$). Fewer studies, however, include the second DOF due to the increase in computational demand.

Until recently, empirical models were more successful in predicting cross-flow displacements and riser curvatures than CFD based codes [12, 11]. The modeling problem is not easy with CFD due to the complexity of flows, the various modes of excitation in a long riser, and the large computational domains required. Frequently CFD of a section (or slice) of riser is coupled with frequency analysis (such as the industry standard Shear7, [30]) for design and analysis of risers [14].

The problem of selecting the appropriate turbulence model, dimensionality (2D vs. 3D) is an unanswered question in the field and an issue this thesis addresses in later chapters. It is generally agreed that two-dimensional models are insufficient to accurately predict VIV and that three-dimensional models

are necessary [8, 26, 23]. However, two-dimensional flows can be sufficient to determine global parameters, such as drag and lift, which are important input parameters for frequency analysis software [1, 19]. While direct numerical simulations (DNS) of the Navier-Stokes equations are ideal, they are incredibly expensive (from a computational standpoint) at the Reynolds numbers of interest, O(Re) =10e4 –10e6. DNS of flow around a cylinder have been run as high as Re=10,000 [15], but DNS has not been run for cylinders with VIV suppression devices. Generally, it is agreed that Reynolds averaged Navier-Stokes (RANS) or unsteady-RANS (URANS) are insufficient for modeling VIV and that large eddy simulation (LES) modeling is optimal if DNS is either not feasable (or not available) [10, 1, 14].

### 1.2.2 Modern VIV Suppression

Today, the most common solutions for VIV suppression are helical strakes (e.g. figure 1.2 [4]), splitter plates (e.g. figure 1.3 [6]), guide foils (e.g. figure 1.1 [17] and [16], ), and fairings (e.g. figure 1.4 [4]). Splitter plates, guide foils and fairings streamline flow in order to reduce the size of vortices while they are adjacent to the cylinder. Streamlining the flow has the effect of delaying separation and shedding. Strakes disrupt the correlation of vortex shedding along the cylinder span, thereby reducing the vortex strength and the magnitude of oscillatory forces [4].

Assi et al. [6], inspired by Grimminger [17], worked with splitter plates and found them very effective at suppressing VIV and reducing drag. They

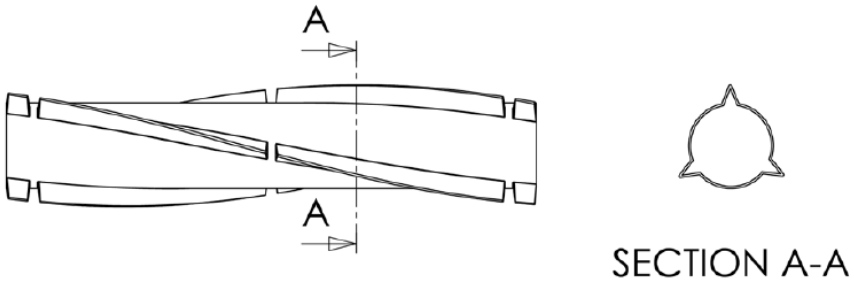


Figure 1.2: Schematic of typical helical strake for VIV suppression, three starts a 0.25D strake height and a 17.5D pitch per start (from [4])

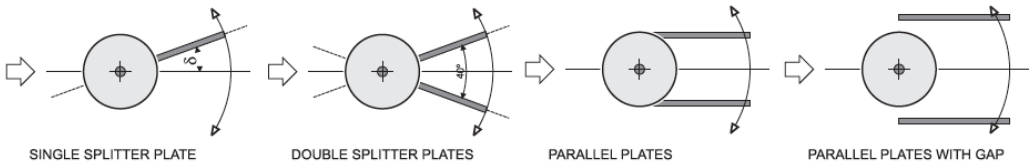


Figure 1.3: Schematic of several spitter plates for VIV suppression (from [6])

suggest that an important parameter in the problem is the torque required to rotate or weathervane the suppression device into the direction of flow. Too large a torque threshold, and galloping resulted, whereas too small a torque threshold resulted in ineffective VIV suppression [6].

Helical strakes were an accepted form of VIV suppression for many wind applications [31] and by the early 1980s were applied to offshore structures [33]. Today they are a popular choice when drag is not a primary concern (e.g. production tubulars). Unfortunately, marine growth quickly reduces the efficacy of strakes, and cleaning costs can be large, as they frequently require

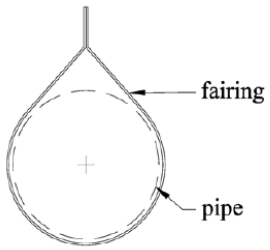


Figure 1.4: Schematic of typical fairing for VIV suppression with a nominal chord of 1.5D (from [4])

an ROV in offshore applications [27, 2].

Fairings have consistently been found to suppress VIV and reduce drag, but they are frequently more expensive both in terms of installation and hardware (fairings must weathervane in line with the flow) [4]. However, fairings require far less maintenance as marine growth does little to reduce their efficacy [2]. Fairings can also provide significant damping when applied to large sections of the tubular [2]. In situ work by Tognarelli et al. [28] documented VIV occurring in bare marine risers and suppression of VIV in faired risers, under similar current regimes.

Despite the apparent advantages of fairings, due to the nature of flow regimes at depth versus the surface, strakes can be a more appropriate choice near the surface due to the oscillating flow directions induced by wave motion [29]. A popular riser design is a hybrid of strakes and fairings with strakes at the surface extending perhaps to a depth of 100 ft and fairings covering the rest of the riser requiring VIV suppression [4].

Ultimately, cost is often a deciding factor in riser design for offshore structures. With rig operating costs upwards of $1,000,000 per day non-productive time is avoided by all means. This means that if overall rig time can be saved by installing a VIV-suppression device (which would allow operation in higher currents, for example), VIV suppression is more likely to be utilized. This brings us back to our discussion of modeling VIV. The ability to predict VIV is of the utmost importance in efficient riser planning and design. Currently, the industry has satisfactory suppression devices, however, largely unanswered questions are when to install VIV-suppression and what percent coverage over a riser is needed, given an expected current regime [7, 4]. There exist some CFD/frequency analysis approaches, but much of the decision-making is empirically based, with retrofitting operations regularly occurring when the riser design was insufficient to prevent VIV. Retrofitting requires rig time, whereas pre-installation (especially on-shore) is far less expensive [5, 2].

In the field of VIV suppression of marine risers, several solutions have been shown to reduce and suppress VIV. Popular solutions include fairings, helical strakes, and splitter plates. Current challenges to the field include adequately modeling the phenomenon of VIV for bare cylinders and cylinders with suppression devices in order to more efficiently design a riser system without the need for retrofitting or for stopping operations due to excessive VIV. LES appears to be the best candidate for accurately modeling tubulars with large aspect ratios (i.e. for deepwater and ultra-deepwater operations). However, the development of better two-DOF and continuous fluid-structure interac-

tion models is still required. Towed tank tests, while common for shallower depths and general VIV suppression testing, are unable to replicate the aspect ratios of deepwater operations. Increased utilization of CFD therefore holds the greatest potential for efficiently and safely determining VIV-suppression requirements for the offshore industry. For these reasons this thesis will explore the efficacy of 2D CFD as a fast and inexpensive method for aiding in the design of suppression devices for marine fairings by comparing numerical predictions (CFD) to experimental results (PIV).

# Chapter 2

# Particle Image Velocimetry

## 2.1 Methods

The PIV experiment was performed with a Dantec Dynamics open channel flume in the Fluids and Hydraulics Lab at the University of Texas at Austin (see Fig. 2.1). The flow-field downstream of the cylinder was captured with a two-dimensional PIV system which was comprised of a Nd:YAG laser and a NanoSense Mk III CCD camera taking images at 500Hz in single frame mode. The water was seeded with 10$\mu$m diameter, silver-coated, hollow glass spheres. A uniform inflow of $\approx$ 0.3-0.35 m/s was used around a cylinder of 0.018m (Re $\approx$ 5400-6300). The cylinder or fairing is set across the span of the flume, perpendicular to the flow and above the boundary layer (cylinder shown in Fig. 2.6 and replica of flume geometry in CFD mesh –cross-section– shown in Fig. 3.4 with a close-up of the cylinder in Fig. 3.5). For each run, the length-scale (for correlating velocity vectors from the images) was calibrated with images of a ruler in the path of the laser (Fig. 2.2). Subsequently, the flow images (without the ruler) were analyzed to create velocity flow-fields in Dantec Dynamics PIV software, DynamicStudio, version 3.40.82.

To determine the optimal method for generating the velocity flow-fields

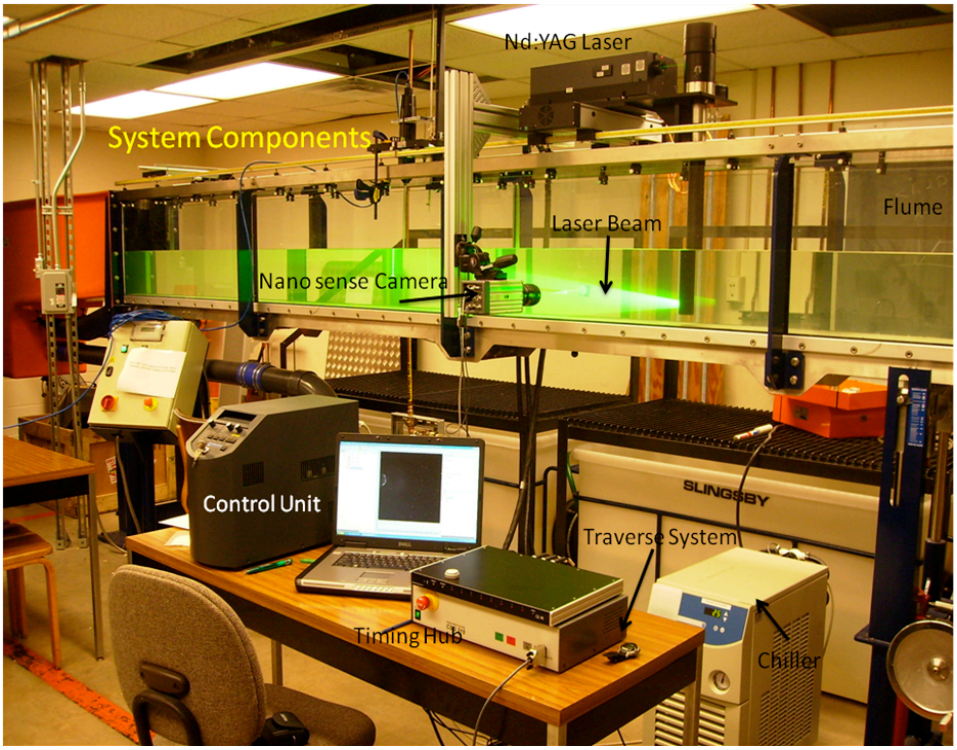


Figure 2.1: Dantec Dynamics flume and PIV setup

in DynamicStudio, several methods were explored with a uniform inflow and no cylinder (Fig. 2.3 shows a snapshot of particles and Fig. 2.4 shows the corresponding vector field). Several camera speeds were tested: 500 Hz, 250 Hz, 100 Hz, and 50 Hz. Also, several correlation methods and interrogation area sizes for the correlation between images and velocity flow-fields were tested within DynamicStudio. A camera speed of 500 Hz in single frame mode best captured the flow at Re 5400-6000. Both the adaptive correlation and adaptive PIV methods for generating velocity vectors from the PIV images were successful, however the adaptive PIV methods proved optimal, even though it

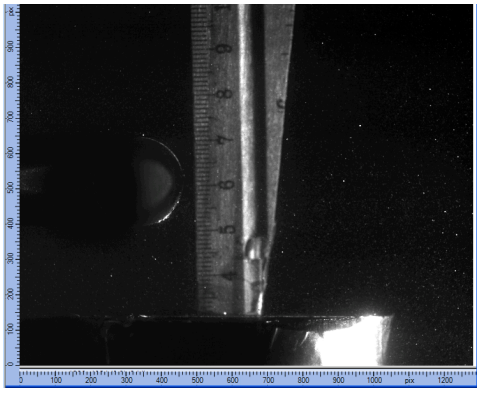

Figure 2.2: PIV calibration image

was considerably more time consuming. The adaptive PIV method iteratively optimizes the size and shape of each interrogation area to better adapt to local flow gradients and seeding densities. The following settings were found to provide accurate velocity fields as suggested by Dantec Dynamics [13]: 16x16 pixel grid step size, a low pass Gaussian filter (k=3), peak height validation (minimum = 0.15), peak height ratio validation (minimum = 1.15), and a S/N ratio (4.0). Universal outlier detection is not optional with the method and used a 5 pixel by 5 pixel neighborhood with an acceptance limit of 2. Vectors were validated after the last iteration. This produced an accurate depiction of the flow when the cylinder was added. Less finely resolved and less filtered methods were found to produce too many erroneous vectors. More finely resolved or more filtered methods did not greatly increase the accuracy with which the flow was represented relative to the increases in computational time required. Also, over-filtering led to removal of data and flow-complexity.

Settings were adjusted to avoid this.

The horizontal velocity with time is shown for a point within the domain (Fig. 2.5). The mean horizontal velocity across the entire domain in the no-cylinder case (0.45 m/s with a standard deviation of 0.01m/s) was used to normalize subsequent PIV runs. The standard deviation of 0.01 m/s is $\approx 2\%$ of the mean horizontal velocity. This value was used in the CFD runs as the free-stream turbulence intensity (specified in Fluent as turbulence intensity, a percent, rather than as turbulent kinetic energy, k). By using this value as the free-stream turbulence parameter, we make the assumption that the standard deviation from the mean represents flow turbulence; some of the variation from mean flow could instead represent inaccuracy in the PIV measurement. Because accuracy of the PIV measurement was difficult to quantify (personal communication with Dantec Dynamics representatives), after careful setup and good visual agreement between flow fields pictures and associated vector fields, we made the assumption that the basic uniform flow case was correctly measured. This is a potential source of error in the experiment.

While the boundary layer was not measured explicitly as part of this experiment, previous work by Han et al. [18] found the boundary layer in the flume to be ≈3cm at the location of the cylinder (Fig. 2.7).

## 2.2 Uniform Flow With Cylinder

The cylinder is shown in figure 2.6. The cylinder is 18mm in diameter and spans the width of the flume (≈30cm). A schematic of the cylinder in

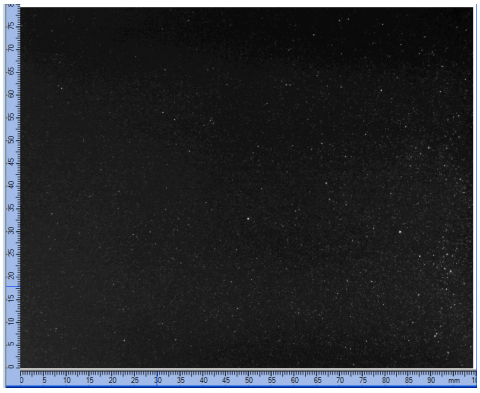

Figure 2.3: PIV image: particles without cylinder

the flume is shown in figure 2.7. Figure 2.8 shows a masked image used for calculating vectors. Figure 2.9 shows a typical snapshot of the vector field around the cylinder.

### 2.2.1 Cross-Stream Comparison

The cylinder was placed perpendicular to the stream and the flow downstream to the cylinder was recorded for three second durations. Flow was recorded in the center of channel plane as well as at 1/4 width distances. In total, flow was measured downstream of the cylinder at three locations in the cross-stream direction (Fig. 2.10).

Time histories of horizontal and vertical velocities were fit via an eighth order Fourier transform using the curve fitting toolbox in Matlab. As an example see figure 2.11, where the raw horizontal velocity time history (at point plus1 in the center of the flume, Fig. 3.6) is shown with the Fourier fit

Figure 2.4: Vectors generated for uniform flow without cylinder

to the data. The eighth order Fourier fit produced an adjusted $R^2$ of 0.58 and a root mean squared error (RMSE) of 0.07, where the adjusted $R^2$ is the degree-of-freedom adjusted coefficient of determination. The observed frequencies of $\approx 4$ cycles per second correspond to an inflow velocity of $\approx 0.36$m/s. This is within the bounds of calculated flow speeds (based on flow rate, width of the flume, and water depth) for the PIV experiments.

In order to examine the effect of three-dimensional structures on two-dimensional flow, we compared Fourier transformed velocity time histories from three slices along the cylinder in the cross-flume direction. Figure 2.12 compares the horizontal velocities from cross-stream slices for point PLUS1 (Fig. 3.6) (adjusted $R^2$ values were 0.58, 0.64, and 0.72 and RMSE were 0.027, 0.016, and 0.020 for the central channel, 1/4 channel, and 3/4 channel horizontal profiles, respectively) were and figure 2.13 shows the same for the vertical velocities at point plus1 (adjusted. $R^2$ values were 0.59, 0.59, and 0.69

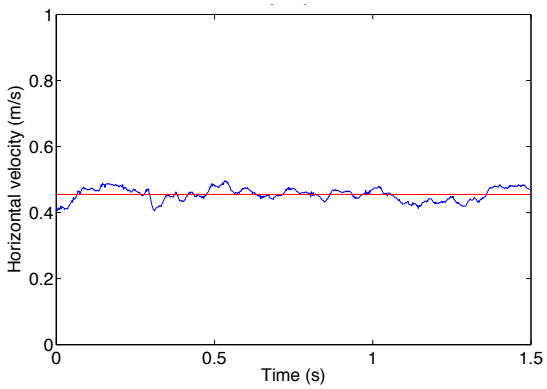


Figure 2.5: Time history of horizontal velocity at point near center of domain (blue) with mean noted (red) for open flume without cylinder or fairing.

and RMSE were 0.031, 0.016, and 0.020 for the central channel, 1/4 channel, and 3/4 channel vertical profiles, respectively). The horizontal velocities compare reasonably well, both in terms of frequency and amplitude. The phases were not adjusted to match since a uniform adjustment was not obtainable between all the points where velocity was recorded. The vertical velocities also compare well in terms of frequency and amplitude. Table 2.1 shows mean velocities in the horizontal and vertical at each cross-stream location (standard deviations are included, means based on raw PIV data, not fit data). The mean horizontal velocities are very similar and the standard deviations the same order of magnitude. The vertical mean velocities are all close to zero (m/s) and show slight differences. The differences in the Fourier transformed velocities and in the raw mean velocities suggests either there exist differences in the flow between cross-stream measurements since the measurements were taken individually (i.e. a differences in pump-speed and Re, a possibility), or

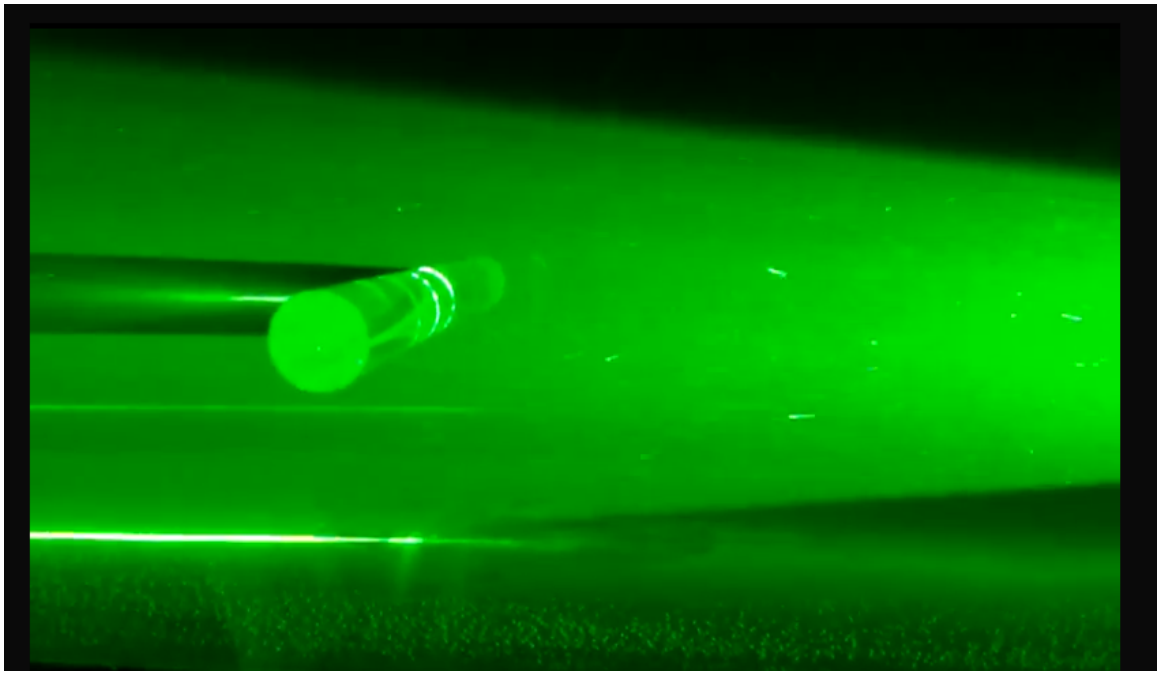

Figure 2.6: Cylinder during measurements, flow is from the left, the laser beam originates to the right

more likely that there are three-dimensional aspects to the flow that are not captured by individual two-dimensional slices.

## 2.3 Uniform Flow With Cylinder and Fairing

The fairing tested is shown in figure 2.14. It was designed to replicate dimensions of a typical fairing that would wrap around the cylinder. Optimal fairing shape and design is a problem worthy of its own thesis and will not be addressed here([3, 5]). The fairing fabricated for this work was designed such that the chordlength to thickness ratio was greater than 2 as fairings with such

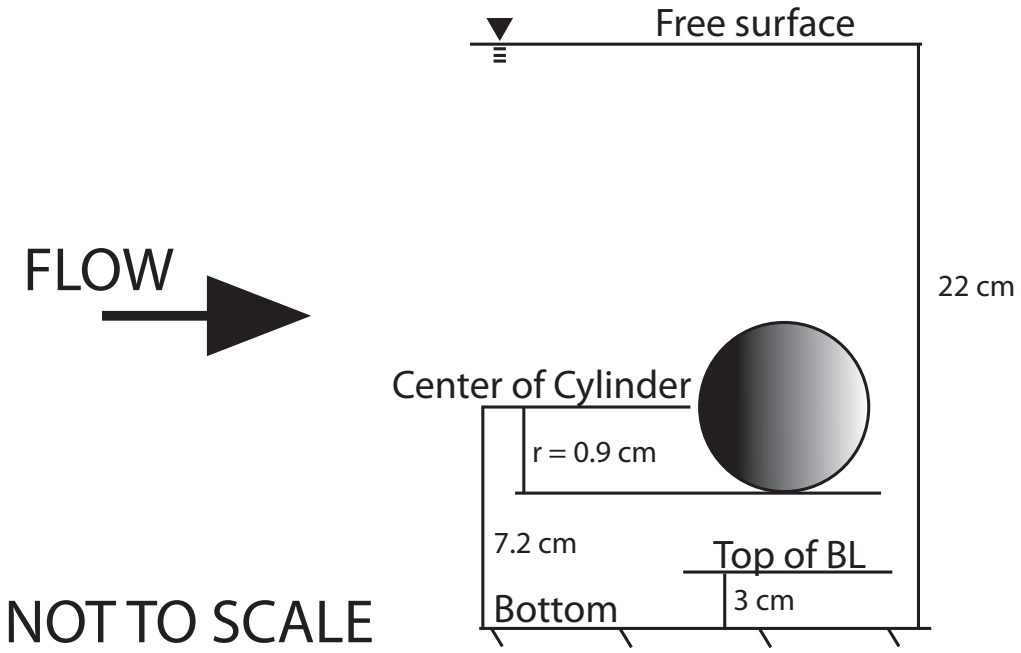


Figure 2.7: Schematic of cylinder in the flume. Not to scale

a ratio were found to reduce both drag and VIV relative to the bare cylinder to which the fairings were attached ([3]). For this experiment the fairing length was 52mm with a thickness of 24mm at the thickest point.

Figure 2.15 shows a typical vector field generated around the fairing.

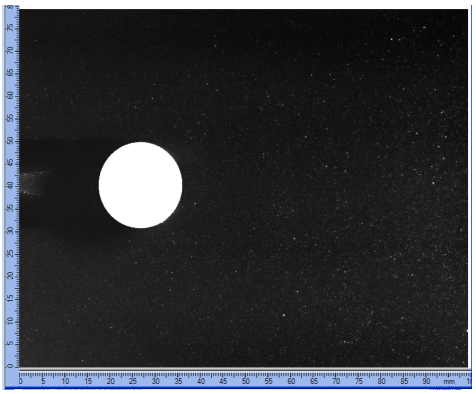

Figure 2.8: Masked cylinder

Table 2.1: Mean velocities at point PLUS1 at cross stream locations

| U or V | cross-stream location | mean velocity | stdev |
|---|---|---|---|
| u | center | 0.3608 | 0.0416 |
| u | 1/4 channel | 0.3658 | 0.0270 |
| u | 3/4 channel | 0.3620 | 0.0367 |
| v | center | -0.0015 | 0.0489 |
| v | 1/4 channel | -0.0123 | 0.0252 |
| v | 3/4 channel | 0.0132 | 0.0354 |

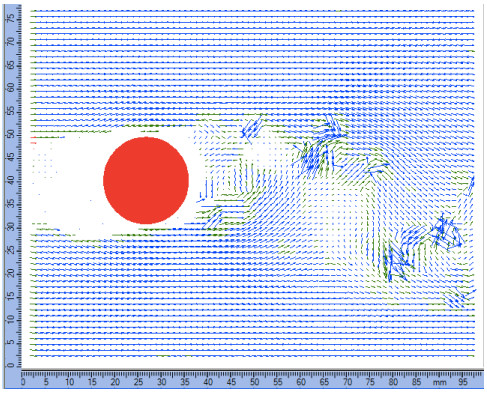

Figure 2.9: Typical vector field around the cylinder. Absence of vectors to left (upstream) of cylinder is due to shading of the laser beam by the cylinder

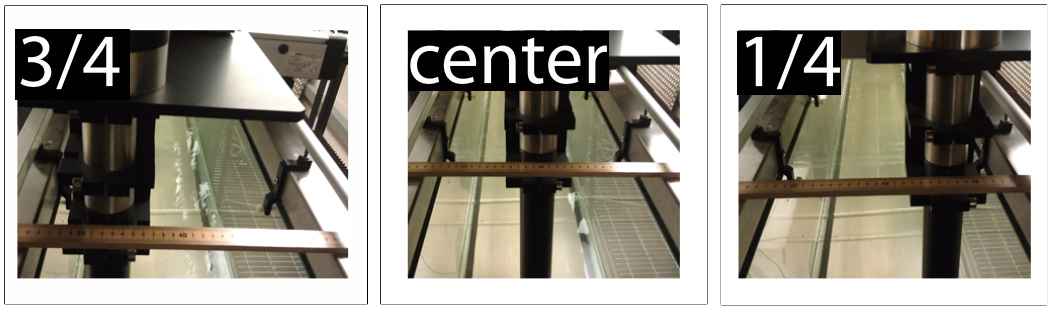


Figure 2.10: Position of laser, looking upstream. Camera is to the left. Flume width is $\approx$ 30 cm

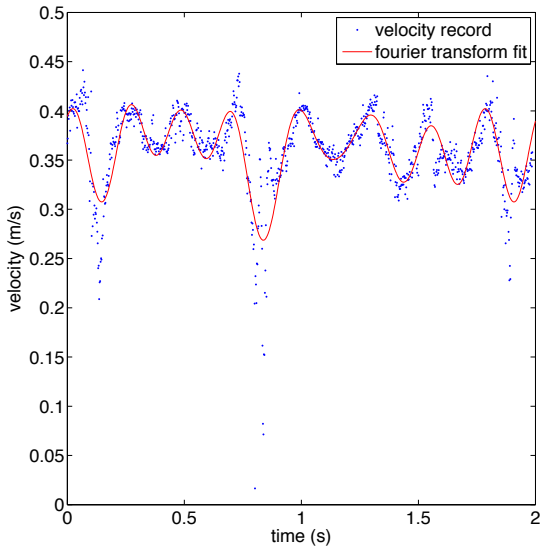


Figure 2.11: Fourier fit to PIV velocity data at point PLUS1

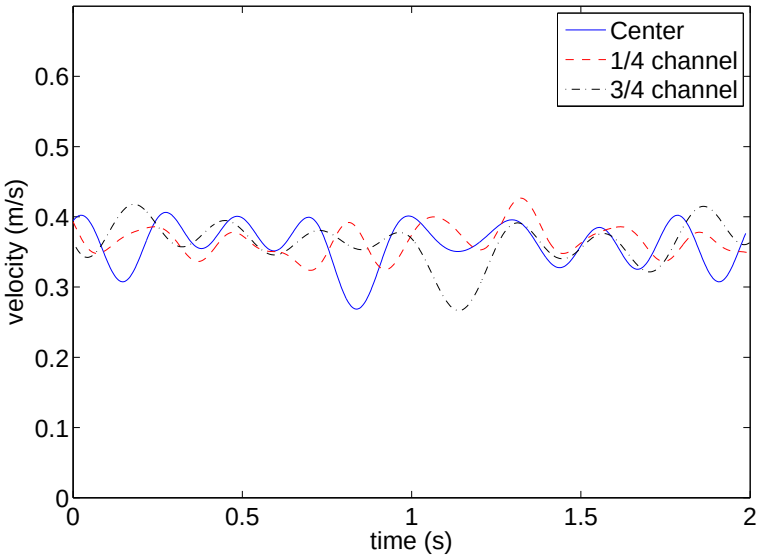


Figure 2.12: Comparison of cross-stream horizontal velocities at point PLUS1

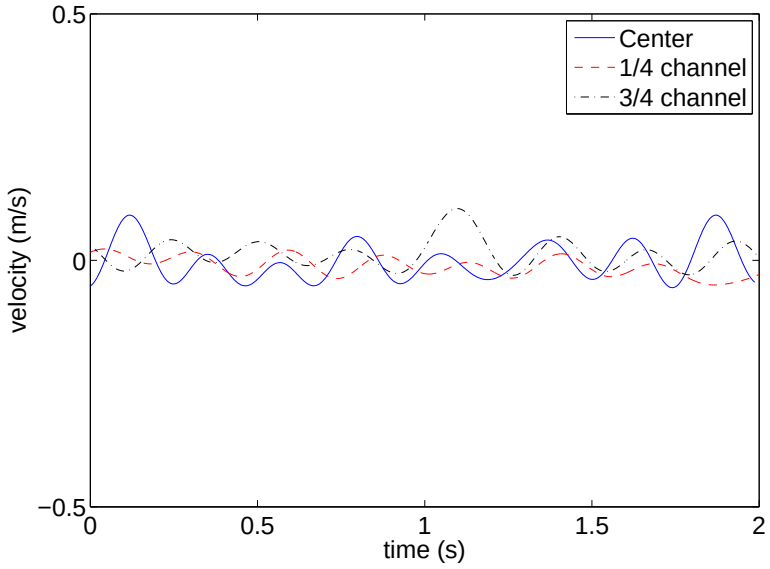


Figure 2.13: Comparison of cross-stream vertical velocities at point PLUS1

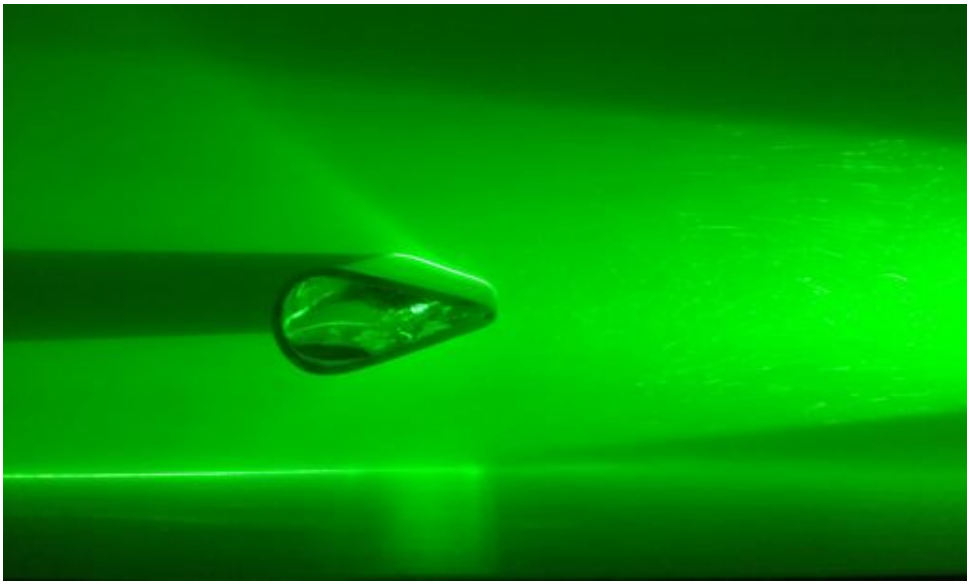

Figure 2.14: Fairing in flume, flow is from the left, the laser beam originates the right

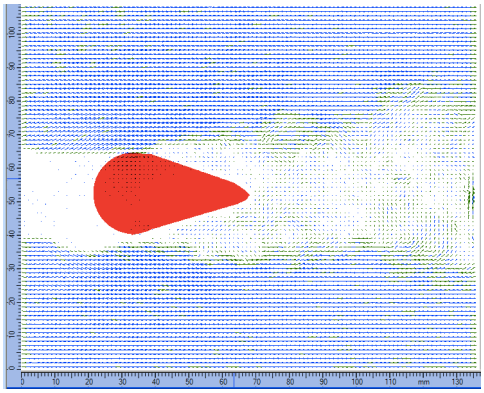

Figure 2.15: Typical vector field around fairing. Absence of vectors to left (upstream) of fairing is due to shading of the laser beam by the fairing

# Chapter 3

# Computational Fluid Dynamics

## 3.1 Cylinder Without Fairing

### 3.1.1 Full Flume Mesh

A mesh replicating the dimensions of the entire flume from inlet to outlet was created in ANSYS ICEM CFD meshing software (see Fig. 3.4 shows a side view of the full mesh, solid blue is dense mesh, not solid wall as made clear in 3.5 which shows a close up of the same mesh near the cylinder). The full-flume domain two-dimensional mesh consisted of 63,000 cells. The boundary condition for the left hand side was an inlet with uniform inflow, the bottom and cylinder were walls, the right hand boundary was an outflow and the upper boundary was a symmetric boundary condition. It was determined that the upper boundary was adequately far enough from the cylinder that additional computational effort and mesh resolution for including a free surface was not necessary. The dimensions of the mesh were normalized to the radius of the cylinder (r=0.009m).

Both RANS and LES simulations were were run in Fluent. Specifically, the RANS runs were unsteady and thus were URANS, however, since all RANS runs were URANS, we will use the terms interchangeably in this work. For the LES runs a uniform width was used to give the two-dimensional mesh

a third dimension (as required by Fluent's LES solver). LES was also run in two-dimensions in Fluent (a forced option) for comparison. Drag and lift coefficients were recorded. They were defined as follows:

$$C_D = \frac{F \times \hat{i}}{\frac{1}{2}\rho u_\infty^2 A} \tag{3.1}$$

$$C_L = \frac{F \times \hat{j}}{\frac{1}{2}\rho u_\infty^2 A} \tag{3.2}$$

where $F$ is the force vector on the cylinder (N), $\rho$ is the density of the fluid (kg/m$^3$), $u_\infty$ is the inflow fluid velocity (m/s), $\hat{i}$ is a unit vector in the horizontal direction, $\hat{j}$ is a unit vector in the vertical direction, and $A$ is the cross-sectional area of the cylinder (equivalent to diameter, $D$).

Lengths were normalized by the cylinder radius ($r = 0.009m$). Time was normalized as follows:

$$t' = \frac{t * u_\infty}{r} \tag{3.3}$$

where $t'$ is the normalized time, $t$ is time (seconds), $u_\infty$ is the inflow fluid velocity (m/s) and $r$ is the cylinder radius (m).

The Reynolds number was calculated as follows:

$$Re = \frac{uD}{\nu} = \frac{0.3m/s * 0.018m}{1e^{-6}m^2/s} = 5400 \tag{3.4}$$

Based on this Reynolds number a Strouhal number of 0.2 is appropriate [24, 9] and as such we would expect a shedding frequency (for the given Re of

5400 as well as for Re in the neighborhood of 5400):

$$f_s = \frac{St * u_\infty}{D} = \frac{0.2 * 0.3m/s}{0.018m} = 3.33s^{-1} \tag{3.5}$$

With our normalization scheme, the normalized shedding frequency would be:

$$f_s' = \frac{St * \frac{u_\infty}{u_\infty}}{\frac{D}{r}} = \frac{0.2 * 1}{2} = 0.1 \tag{3.6}$$

Each CFD run was "ramped-up" for 200 "normalized seconds" (4-5 seconds of real flow time depending on $u_\infty$) to ensure the solution stabilized. URANS simulations were run with a normalized dt of 0.01 (0.2e-3 seconds) which meant 20,000 timesteps. LES runs were run with a normalized dt of 0.005 (0.1 e-3 seconds) for 40,000 timesteps during rampup. Runs were then continued for 60 more normalized time units (≈1.5 seconds of real flow time). During this 60s′ run, variables of interest were recorded. All comparisons, between CFD runs and PIV runs, or between different CFD runs were all made during this post-ramp up timeframe. Runs were computed on a single node of the Computational Hydrodynamics Laboratory server, using 8 Intel Core2 Duo 2.5GHz CPU. Full mesh rampup runs in RANS took about 12.5 hrs clock time (≈100 hrs CPU time). Full mesh rampup in LES took about 100hrs clock time. The RANS simulations were run with a k-$\omega$ SST turbulence model and the LES simulations were run using a Smagorinsky-Lilly subgrid turbulence model.

Velocities were recorded at set points downstream of the cylinder (and fairing) for comparison between RANS, LES, and the PIV (see Fig. 3.6 and

3.7).

The pressure coefficients along the cylinder surface were reasonable in both the RANS (Fig. 3.1) and LES (Fig. 3.3) simulations. The x-axes show degrees from the leading edge of the cylinder. The pressure coefficients are shown at a given point in time, and the area between the two curves represents the lift forces on the cylinder. Since the cylinder is shedding, there is a pressure difference between the top and bottom of the cylinder. Y+ values were less than 0.3 in both cases (for RANS shown in Fig. 3.2). Y+ values along the flume bottom were on the order of 30, which we determined was acceptable, given that our cylinder was above the boundary layer and a smaller y+ on the flume bottom would unnecessarily increase the mesh size and computation time. While an explicit grid-convergence study was not carried out, several meshes were tested in an effort to obtain a reasonable y+ value. For this study we were interested in Re $\approx$5400. With Re of this order of magnitude (provided the y+ values on the cylinder were small enough) varying Re did not greatly affect convergence of the CFD results. Re >10,000 were not tested and Re >8000 are not discussed in this paper due to the physical constraints of the current flume setup and our desire to replicate the flume in CFD.

### 3.1.2 Smaller Domain

Because much of the full mesh, upstream of the cylinder, is uniform and does not affect the flow beyond creating a boundary layer, the use of a smaller domain mesh was investigated. The original mesh was "split" at

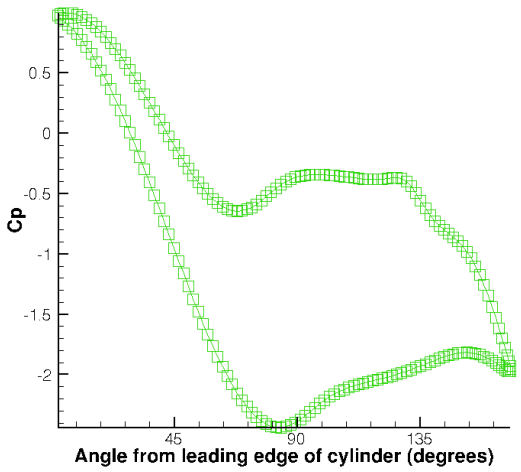


Figure 3.1: Snapshot of $C_P$ RANS. Shapshot was taken while vortex shedding was taking place. Area between curves represents lift forces on cylinder

approximately X=392 (using normalized x coordinates, see figures 3.8 and 3.9). Profiles of velocity (horizontal and vertical), turbulent kinetic energy, and dissipation were extracted from the full mesh using a surface monitor in Fluent. The profiles from the full mesh, taken at the location of the small mesh inlet, were set as the inlet boundary conditions and the smaller domain was run and compared to the full domain. The time dependency of the inlet profile extracted from the full flume mesh was examined and found to be essentially zero. The full cylinder mesh was 63,930 cells, the small domain cylinder mesh was 59,409 cells, and the fairing mesh was 41,653 cells. The smaller domain mesh is exactly the same as the full-domain mesh in the regions were both exist, i.e. downstream of the slice.

The lift and drag coefficients of the full and small domains were com-

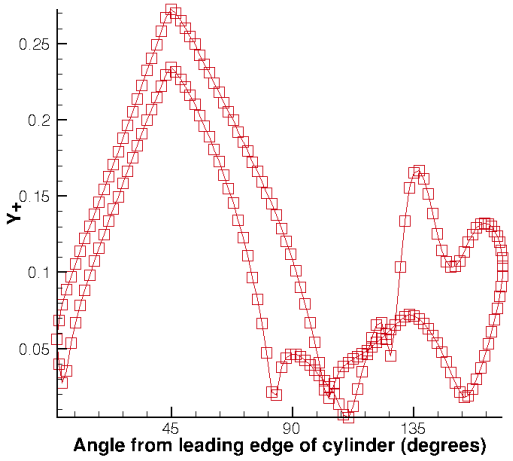


Figure 3.2: Y-plus along the cylinder wall - RANS

pared and support the notion that we can use the smaller domain without sacrificing accuracy (Figs. 3.10 and 3.11). Velocities and pressures (not shown) were also examined and compared equally well.

## 3.2 Cylinder With Fairing

Figure 3.12 shows the mesh used for the fairing simulation. The dimensions are normalized in the same manner as for the cylinder mesh (using cylinder radius). Figure 3.13 shows a closeup of the mesh near the fairing. Values of pressure (Fig. 3.14) and y-plus (Fig. 3.15) were reasonable.

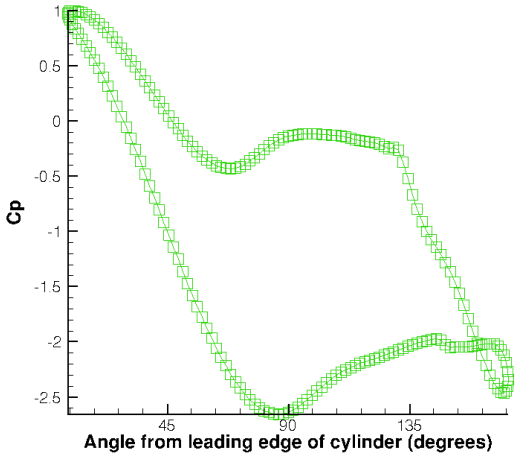


Figure 3.3: Snapshot of $C_P$ LES. Shapshot was taken while vortex shedding was taking place. Area between curves represents lift forces on cylinder

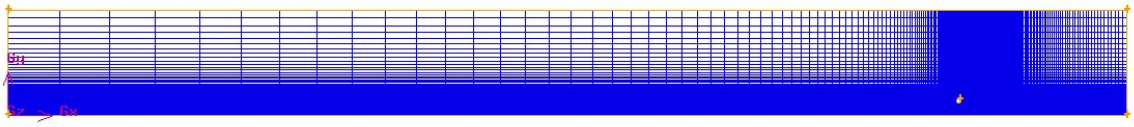

Figure 3.4: Side view (x-y horizontal-vertical plane) of full mesh, replicating dimensions of flume. As clear in close-up figure, areas of solid blue are not solid walls, rather dense mesh

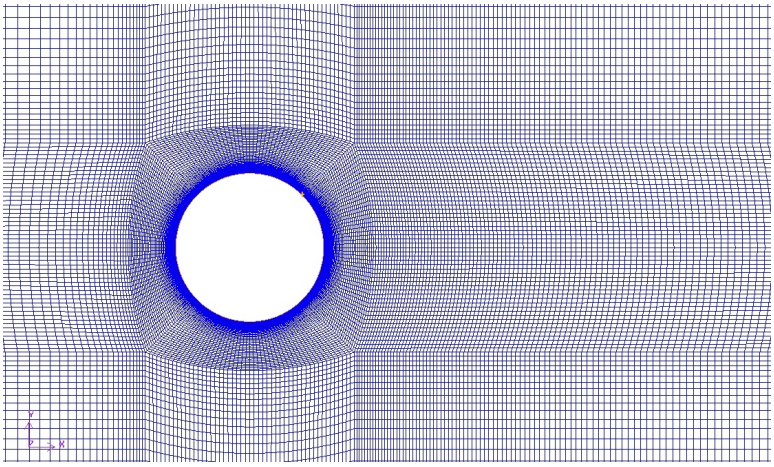

Figure 3.5: Closeup of mesh in vicinity of cylinder

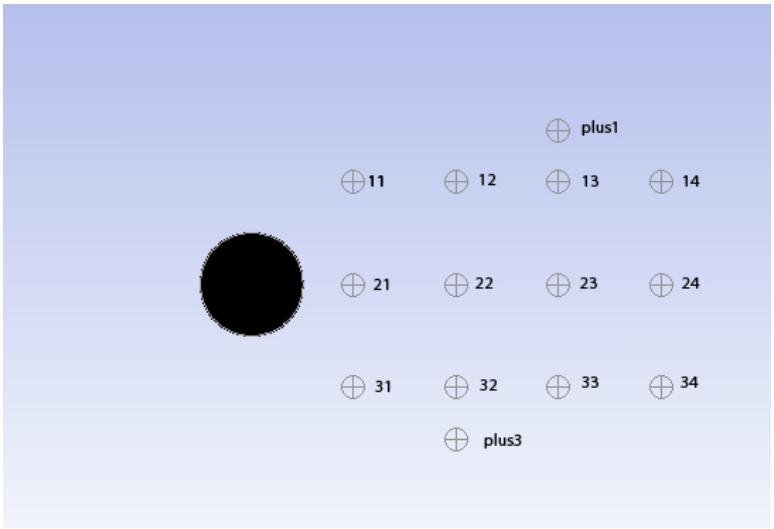


Figure 3.6: Location of velocity-tracking points relative to cylinder

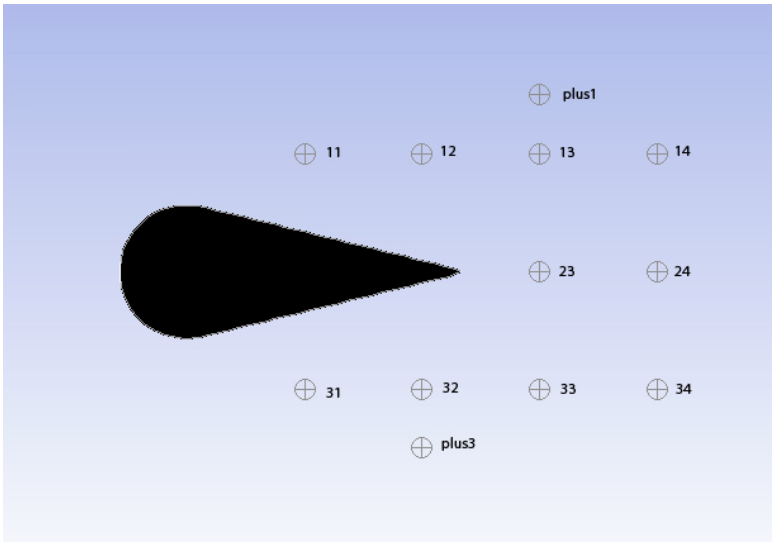


Figure 3.7: Location of velocity-tracking points relative to fairing

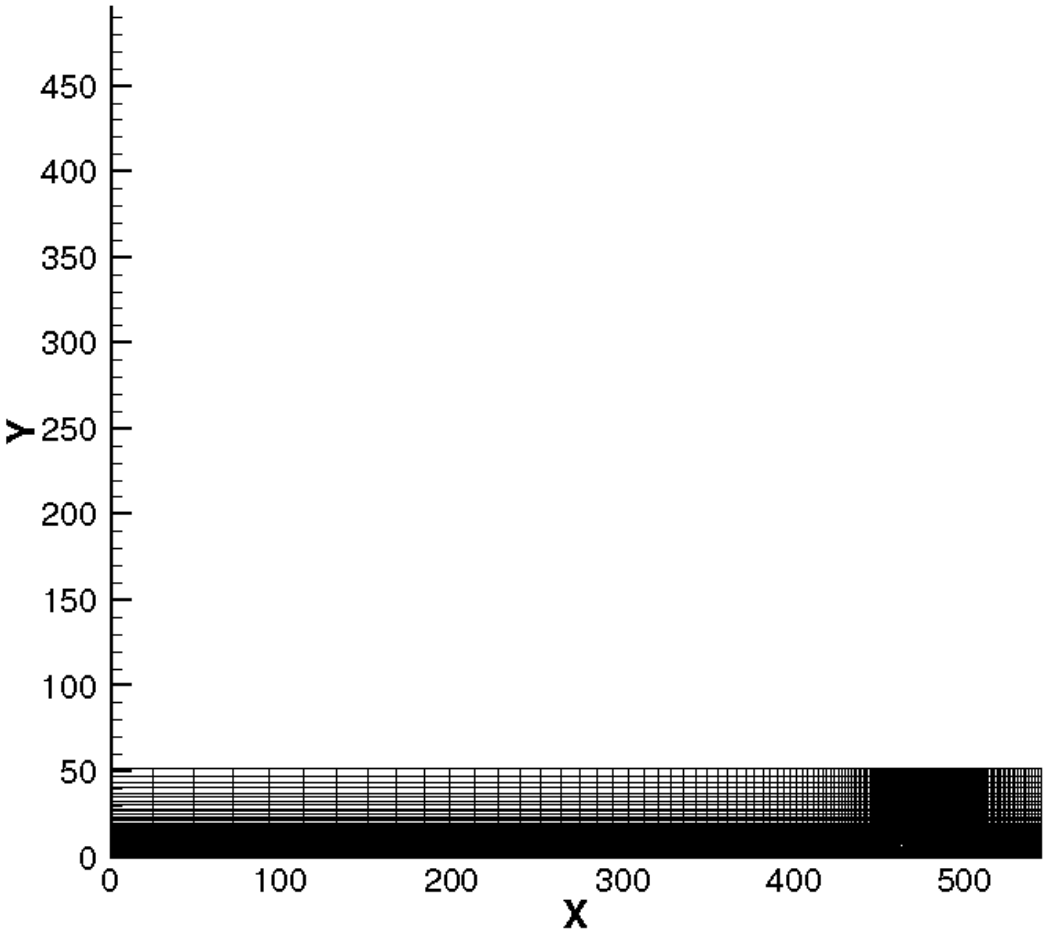


Figure 3.8: Full domain mesh. Cylinder obscured by mesh density. Dimensions are normalized to cylinder radius

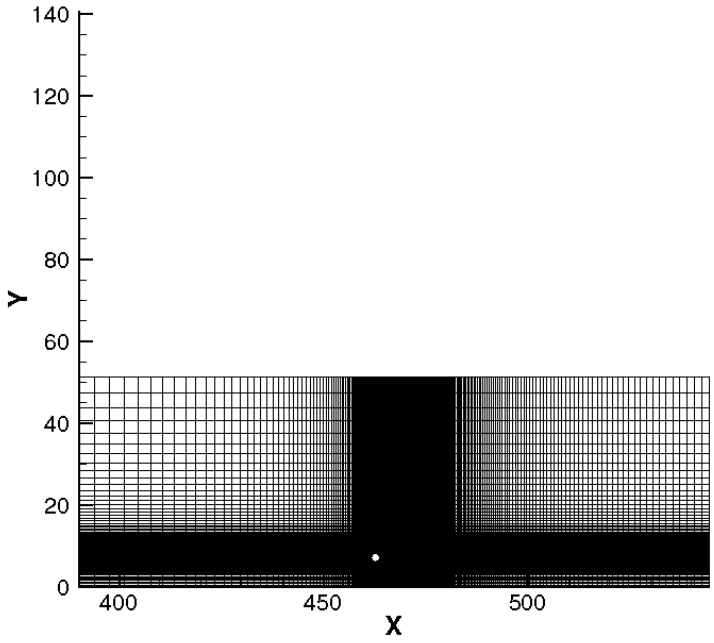


Figure 3.9: Small domain, replicating the full domain from X≈390 to X≈550. Dimensions are normalized to cylinder radius

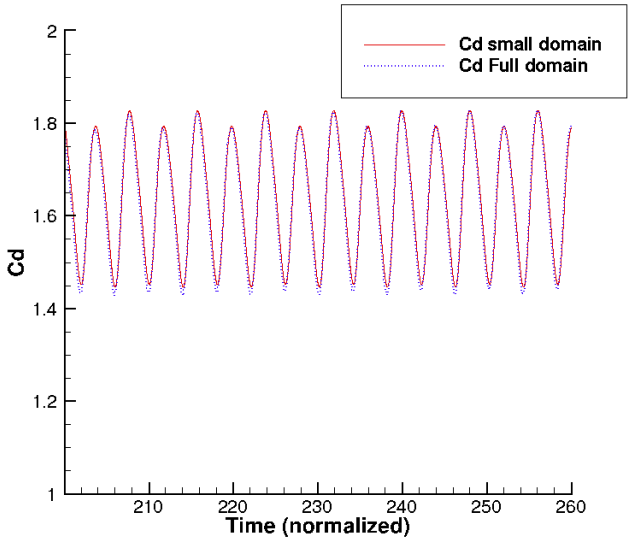


Figure 3.10: Cylinder drag coefficient with time, comparison between full and small domains

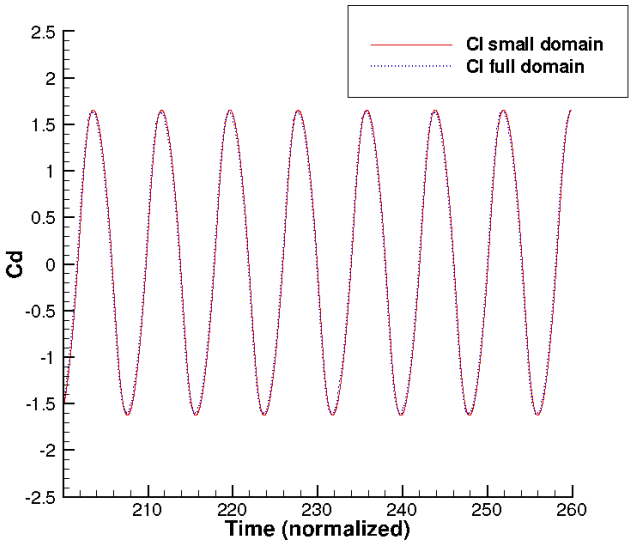


Figure 3.11: Cylinder lift coefficient with time, comparison between full and small domains

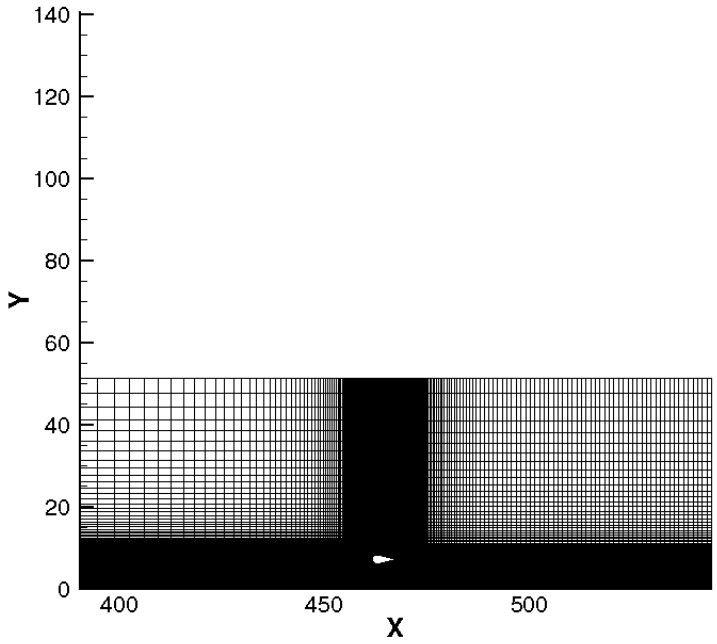


Figure 3.12: Fairing mesh. (Dimensions are normalized to cylinder radius)

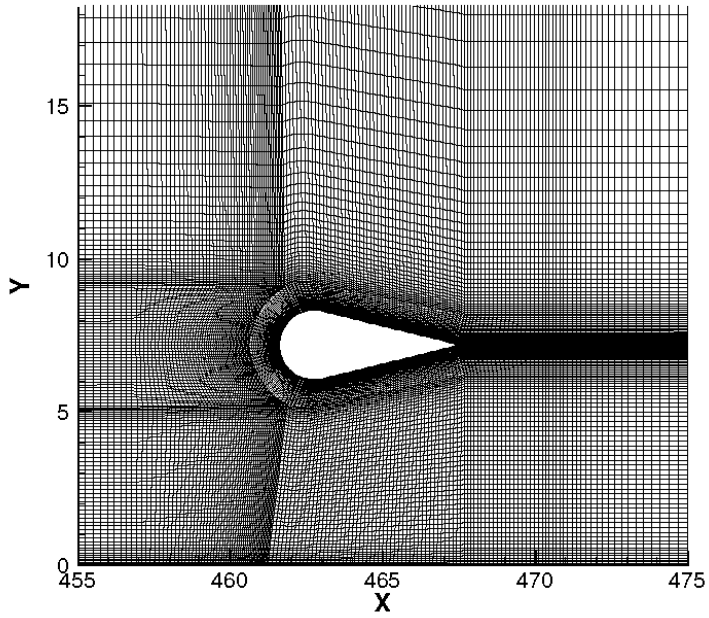


Figure 3.13: Closeup of fairing mesh near the fairing. (Dimensions are normalized to cylinder radius)

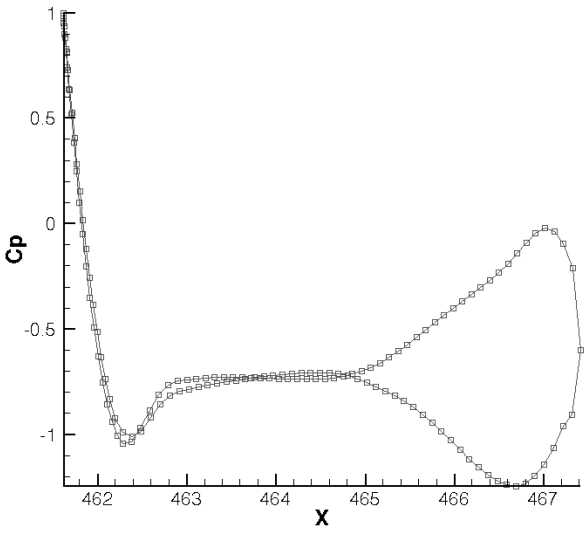


Figure 3.14: Snapshot of pressure coefficent along fairing. Area between curves represents lift forces on fairing. (Dimensions are normalized to cylinder radius)

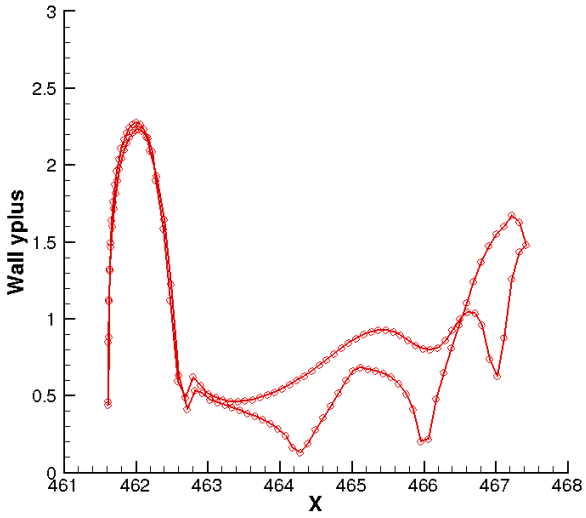


Figure 3.15: Y-plus along fairing. (Dimensions are normalized to cylinder radius)

# Chapter 4

# Comparison of PIV and CFD Flows

## 4.1 Cylinder Without Fairing

### CFD and PIV velocity vector field comparison

Before we compare velocities at specific points, we look at the general trends in the vector fields. While this is more easily accomplished with a video, a series of snapshots that capture the shedding of a positive (counter-clockwise) vortex will suffice. Each snapshot shows velocity vector fields with similar color scale denoting normalized vector magnitude. PIV vectors are on the left and RANS vectors are on the right (Figs. 4.1, 4.2, 4.3, 4.4, 4.5, 4.6, 4.7, 4.8, 4.9, and 4.10). The real flow time interval between figures is $\approx 0.024$ seconds.

This sequence of vector field comparisons shows that CFD captures the general physics of the flow. We see a damping of the turbulence in the CFD as compared to the PIV, as expected by an unsteady RANS run. This results in the CFD predictions showing a smaller region of low and reverse velocities in the wake as compared to the PIV measurements. The shedding pattern is acceptably similar between PIV and CFD and on similar time scales. The region of reverse flow is visibly larger in the PIV flow as compared to CFD

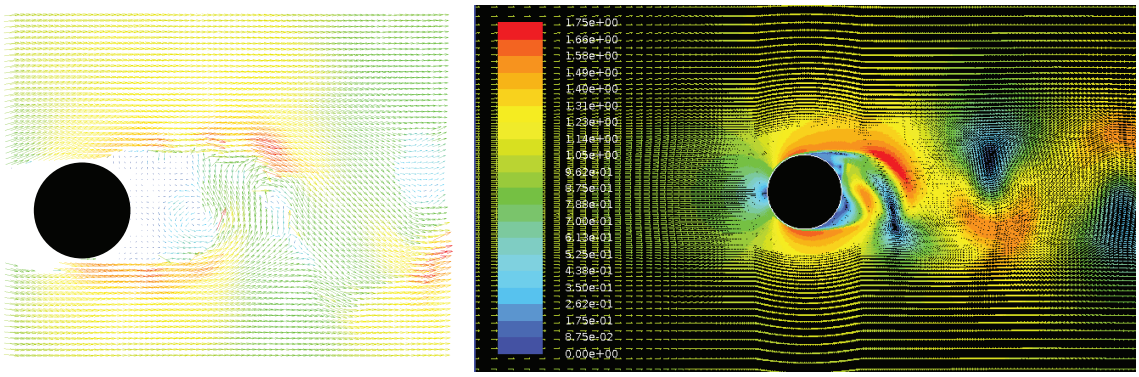


Figure 4.1: Shedding comparison step 1 of 10. PIV (left) and CFD (right). Color scale denotes velocity vector magnitude

flow (Fig. 4.11). The wake zone in general appears to be larger in PIV than CFD. This difference represents a shortcoming of our CFD model.

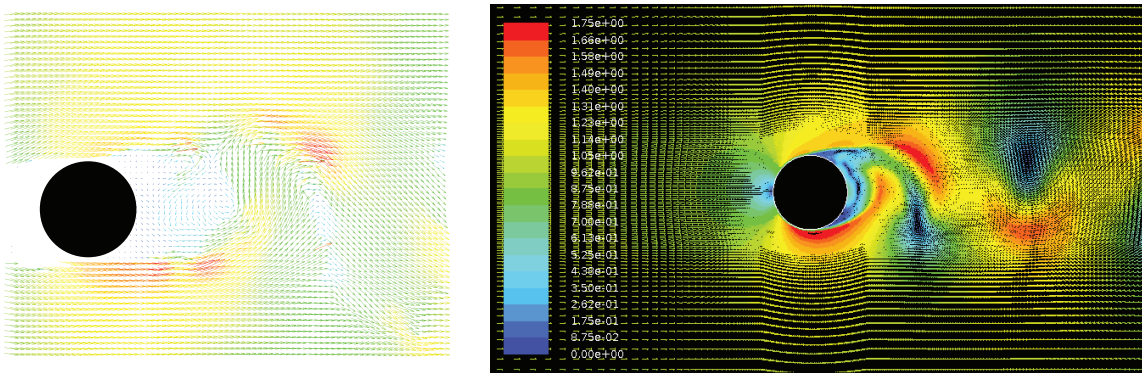


Figure 4.2: Shedding comparison step 2 of 10. PIV (left) and CFD (right). Color scale denotes velocity vector magnitude

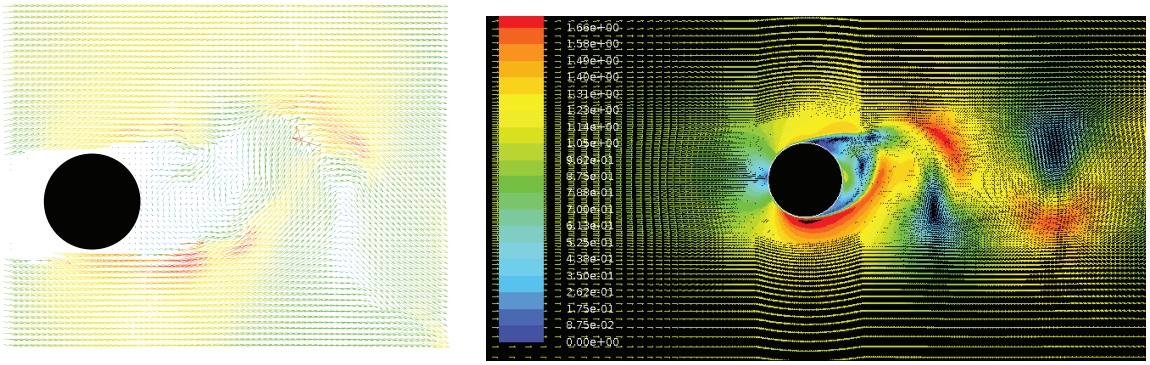


Figure 4.3: Shedding comparison step 3 of 10. PIV (left) and CFD (right). Color scale denotes velocity vector magnitude

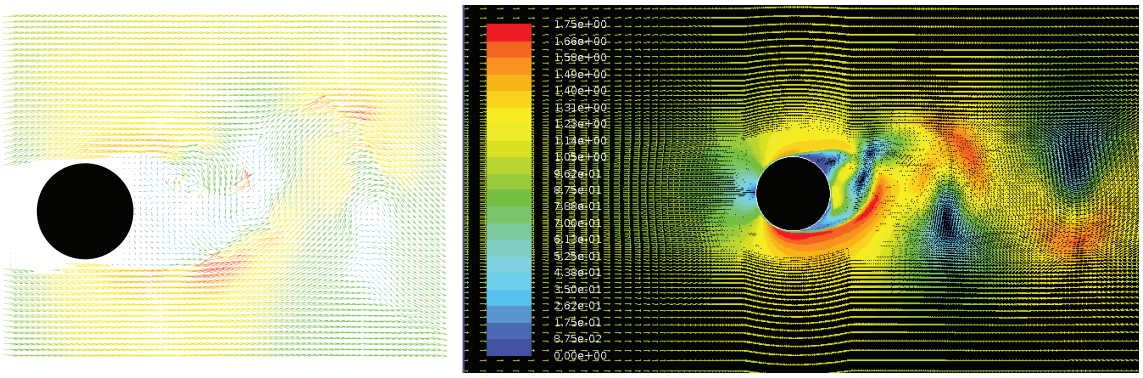


Figure 4.4: Shedding comparison step 4 of 10. PIV (left) and CFD (right). Color scale denotes velocity vector magnitude

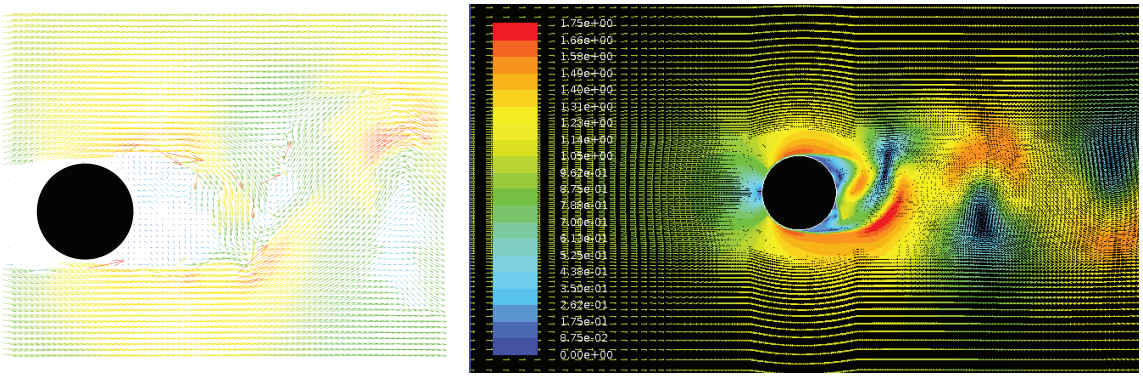


Figure 4.5: Shedding comparison step 5 of 10. PIV (left) and CFD (right). Color scale denotes velocity vector magnitude

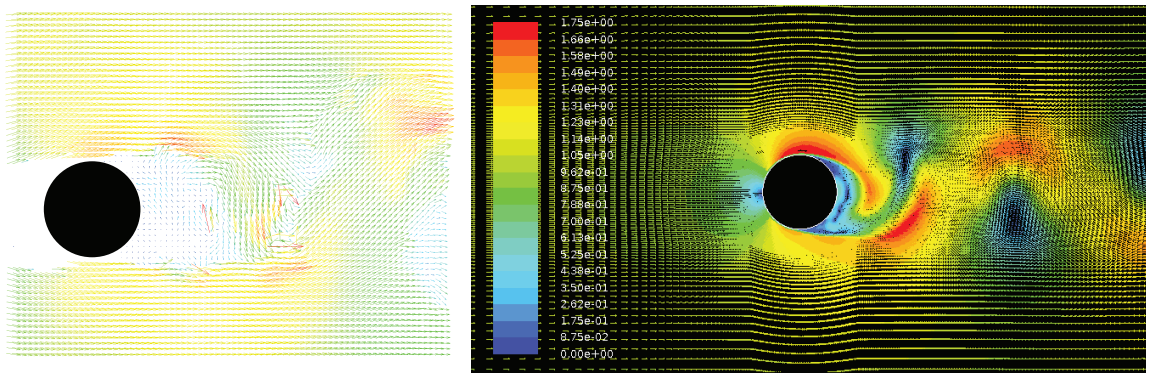


Figure 4.6: Shedding comparison step 6 of 10. PIV (left) and CFD (right). Color scale denotes velocity vector magnitude

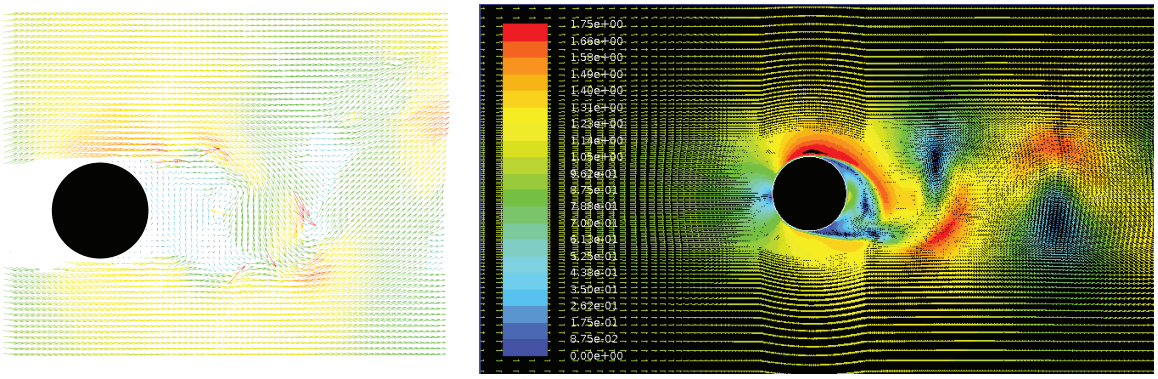


Figure 4.7: Shedding comparison step 7 of 10. PIV (left) and CFD (right). Color scale denotes velocity vector magnitude

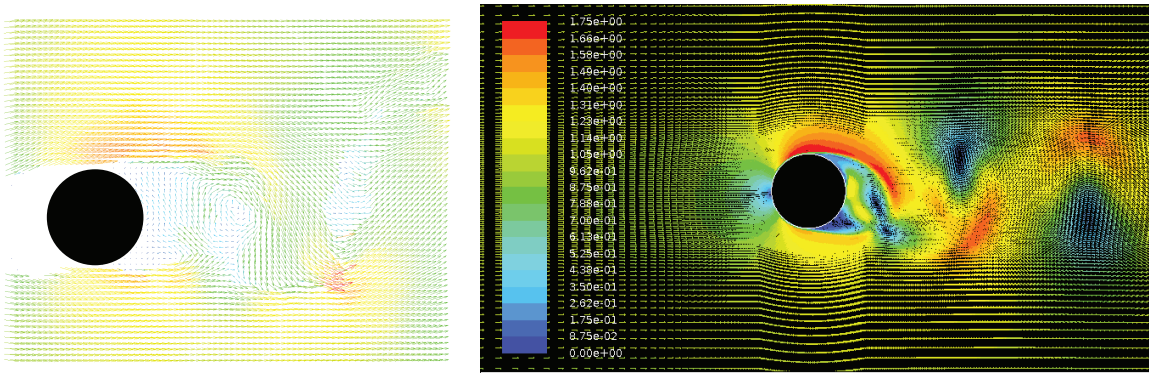


Figure 4.8: Shedding comparison step 8 of 10. PIV (left) and CFD (right). Color scale denotes velocity vector magnitude

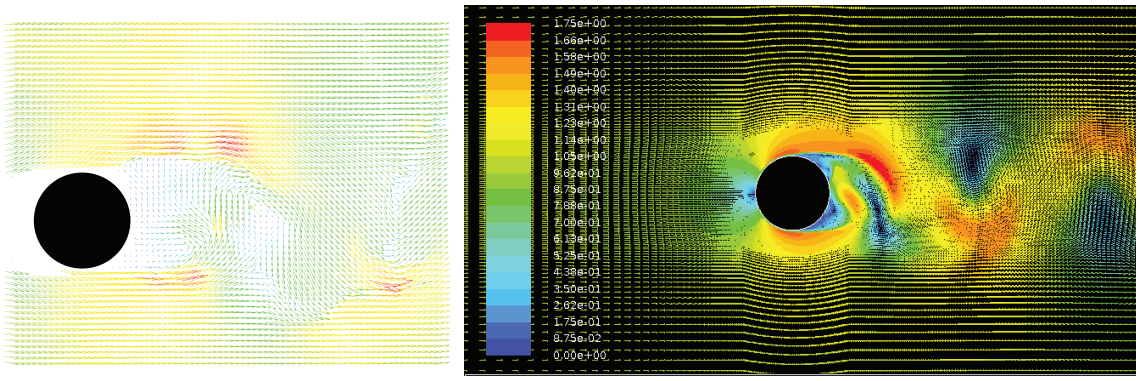


Figure 4.9: Shedding comparison step 9 of 10. PIV (left) and CFD (right). Color scale denotes velocity vector magnitude

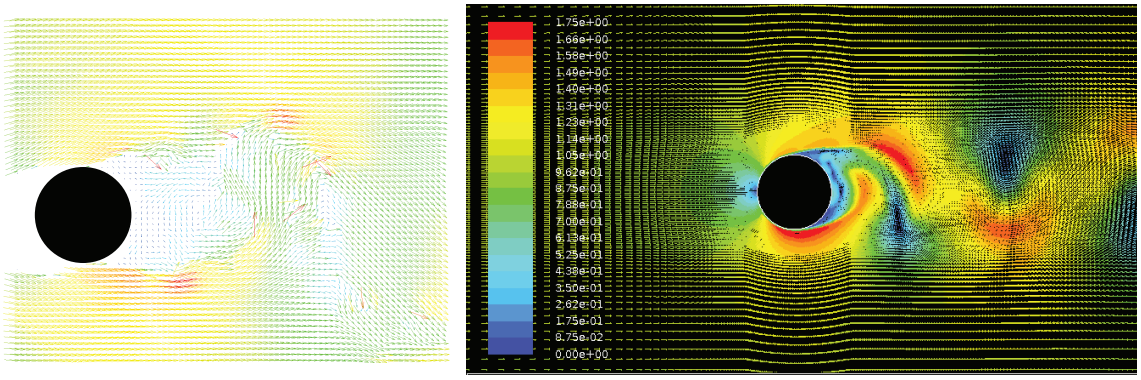


Figure 4.10: Shedding comparison step 10 of 10. PIV (left) and CFD (right). Color scale denotes velocity vector magnitude

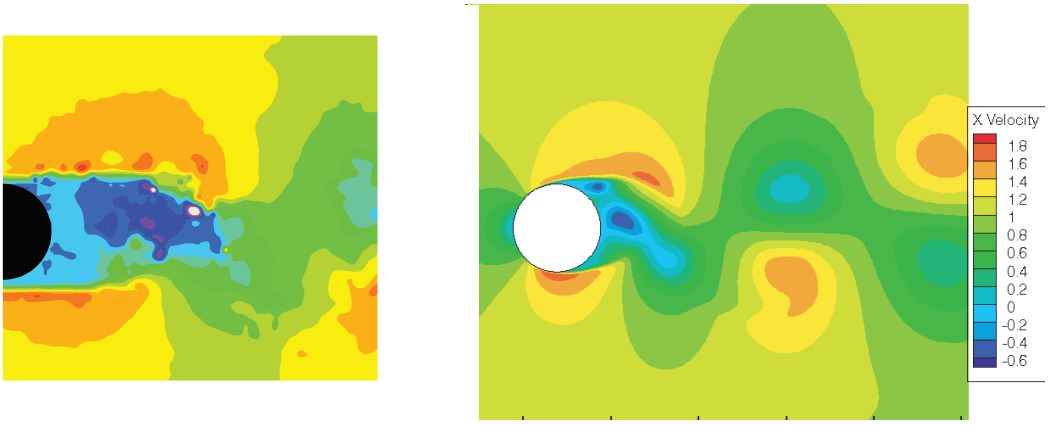


Figure 4.11: Horizontal velocity contours. PIV (left) and CFD (right). Color scale denotes normalized horizontal velocity (Blue areas represent reverse flow. Area to left of cylinder in PIV whited out since velocities there are not valid due to shading.

**RANS and LES velocity comparisons with PIV**

At specific points shared between the PIV and CFD domain, RANS appears to predict the amplitude of the PIV-measured velocity fairly well (Figs. 4.12, 4.13, 4.14, and 4.15). In each figure, the location of the velocity tracking point is noted on the left hand side, and on the right hand side we see the PIV-CFD comparison: the PIV data in blue x marks, an eighth order Fourier transform of the PIV data in black, and the CFD-predicted velocity with time in red. Both time and velocity are normalized as described in section 3.1.1. Agreement between RANS and filtered PIV amplitudes increases as we move away from the cylinder. As we approach the cylinder, RANS tends to over predict the amplitude of the filtered PIV velocity. In figure 4.12 we see a large negative peak around $50s'$. This peak is clearly missed by the RANS steady state solution as one would expect. This is a clear limitation of a RANS approach. At point 11 (Fig. 4.13) the PIV horizontal velocity is on the higher end of the CFD-prediction.

Because a uniform time-adjustment could not be found across the velocity points that put CFD-predictions in phase with the PIV-measurements, no time-ajustment was made. Frequencies do not agree as well as amplitudes, but the frequencies are not wildly different, when the Fourier fitting of the data was reasonable. Associated errors with the Fourier transforms are listed in Table 4.1. The data were normalized prior to error calculations.

We see similar results in the vertical velocities (Figs. 4.16, 4.17, and 4.19). Associated errors are listed in Table 4.2 (Again, the data were nor-

Table 4.1: Error associated with horizontal PIV-filtered velocities. Data were normalized prior to error calculations.

| Point | Adjusted $R^2$ | RMSE |
|---|---|---|
| plus1 | 0.8298 | 0.0904 |
| 11 | 0.7918 | 0.0358 |
| 23 | 0.4225 | 0.1821 |
| 32 | 0.8656 | 0.0594 |

Table 4.2: Error associated with vertical PIV-filtered velocities. Data were normalized prior to error calculations.

| Point | Adjusted $R^2$ | RMSE |
|---|---|---|
| plus1 | 0.7551 | 0.0859 |
| 11 | 0.8156 | 0.0859 |
| 23 | 0.8957 | 0.1955 |
| 32 | 0.8752 | 0.0600 |

malized prior to error statistics calculations). At point 23 (Fig. 4.18) the RANS-predicted vertical velocity captures an extended peak visible in the raw velocity data, but not in the Fourier transformed data. That this high frequency component is visible in the CFD and raw data highlights a moment where CFD accurately captures an interesting phenomenon in the wake of the cylinder. It also warns against the dangers of over-filtering, as the eighth order Fourier fit does not capture the phenomenon.

A similar comparison of PIV-measured and LES-predicted velocities shows that the LES simulation is perhaps more capable of describing some

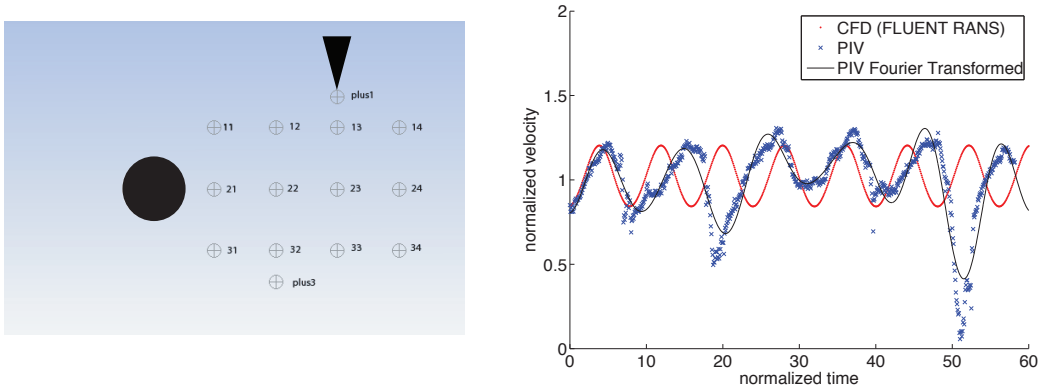


Figure 4.12: Comparison of PIV-measured and RANS-predicted horizontal velocities (with cylinder) at point PLUS1

of the complexities of turbulent flow, and in a general sense captures amplitudes and frequencies measured by PIV (horizontal: Figs. 4.20, 4.21, 4.22, and 4.23); (vertical: Figs. 4.24, 4.25, 4.26, and 4.27). While the turbulent excursions from periodic flow are better captured by LES, the LES runs are very time consuming. We see general agreement in LES results compared to RANS. Figures. 4.28 and 4.29 show RANS, LES, PIV, and PIV fit data for horizontal and vertical velocities, respectively, at point PLUS1. For ease of comparison, figures 4.30 and 4.31 show only the RANS and LES horizontal and vertical velocities, respectively. CFD results tend to over predict the PIV-filtered velocity amplitudes but generally the CFD amplitudes fall within the spread of the recorded PIV data. Frequencies are similar, but always slightly off. Agreement between RANS and PIV and LES and PIV is stronger away from the cylinder.

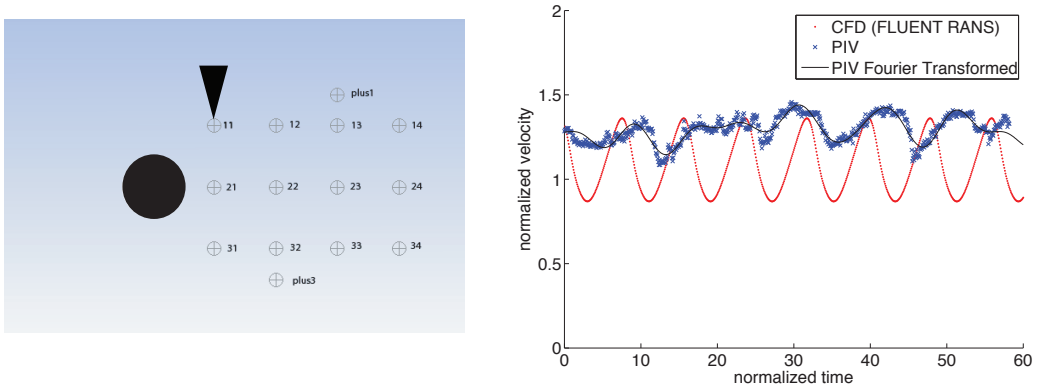


Figure 4.13: Comparison of PIV-measured and RANS-predicted horizontal velocities (with cylinder) at point 11

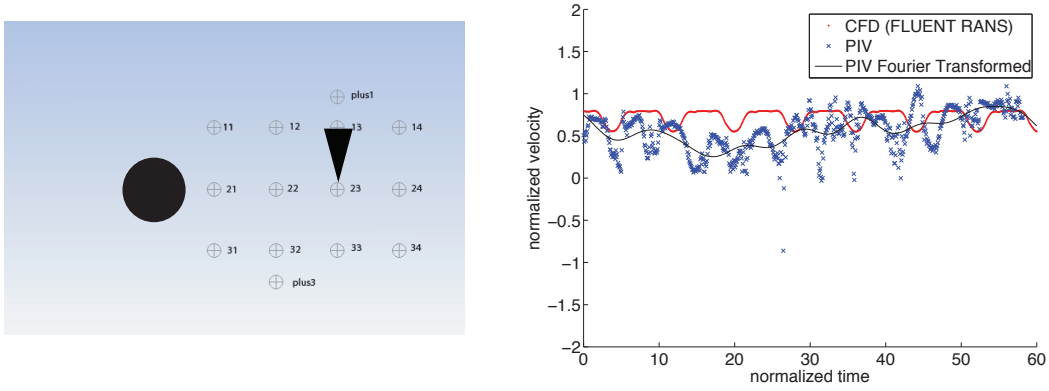


Figure 4.14: Comparison of PIV-measured and RANS-predicted horizontal velocities (with cylinder) at point 23

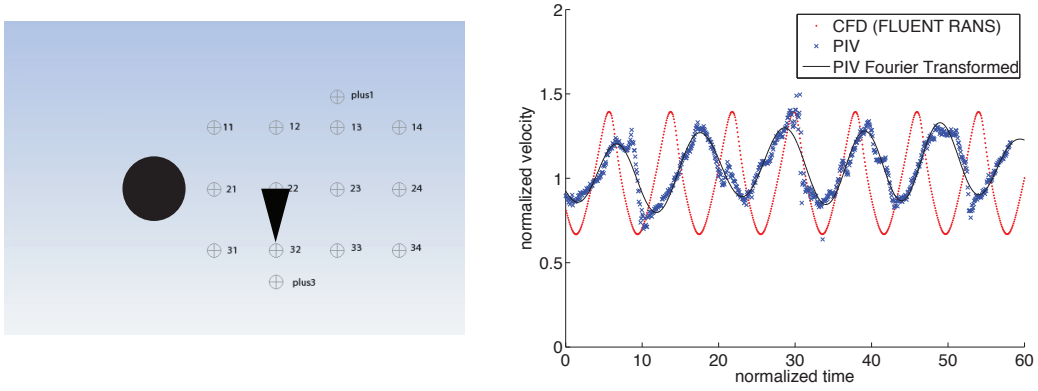


Figure 4.15: Comparison of PIV-measured and RANS-predicted horizontal velocities (with cylinder) at point 32

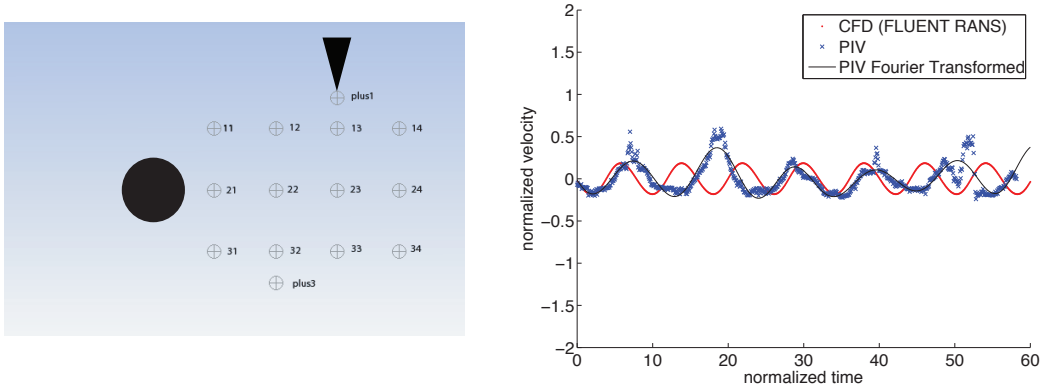


Figure 4.16: Comparison of PIV-measured and RANS-predicted vertical velocities (with cylinder) at point PLUS1

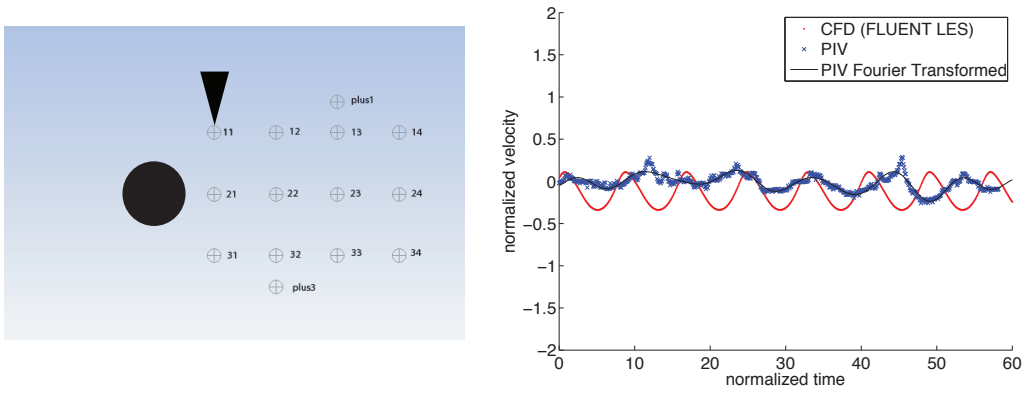


Figure 4.17: Comparison of PIV-measured and RANS-predicted vertical velocities (with cylinder) at point 11

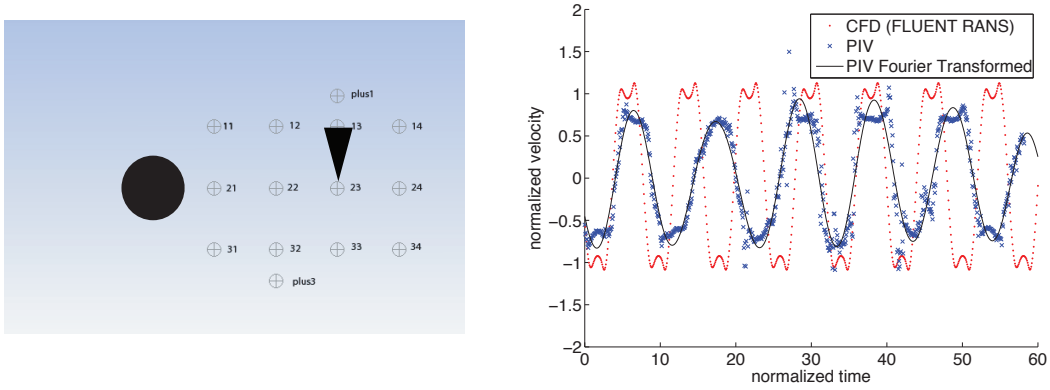


Figure 4.18: Comparison of PIV-measured and RANS-predicted vertical velocities (with cylinder) at point 23

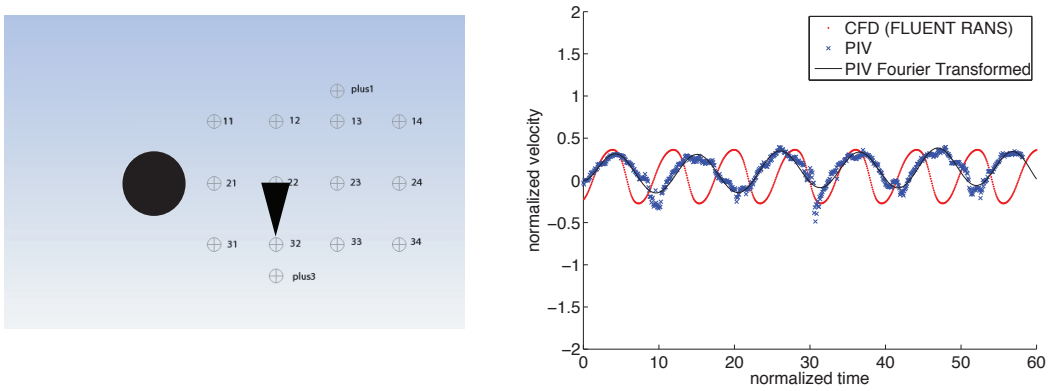


Figure 4.19: Comparison of PIV-measured and RANS-predicted vertical velocities (with cylinder) at point 32

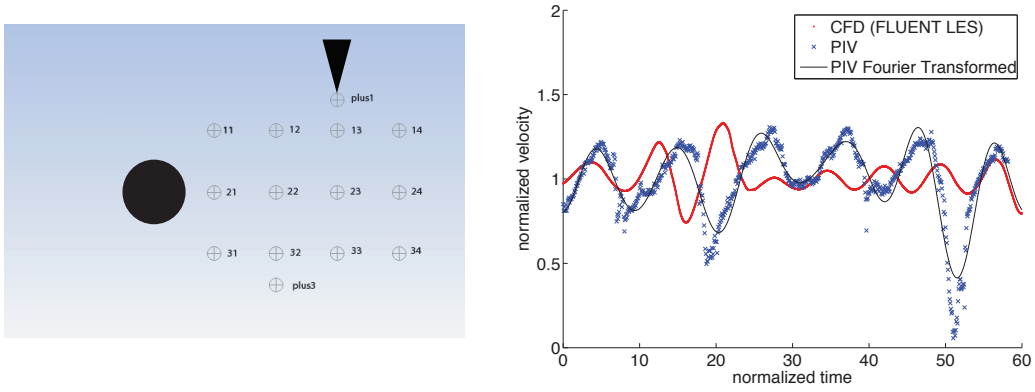


Figure 4.20: Comparison of PIV-measured and LES-predicted horizontal velocities (with cylinder) at point PLUS1

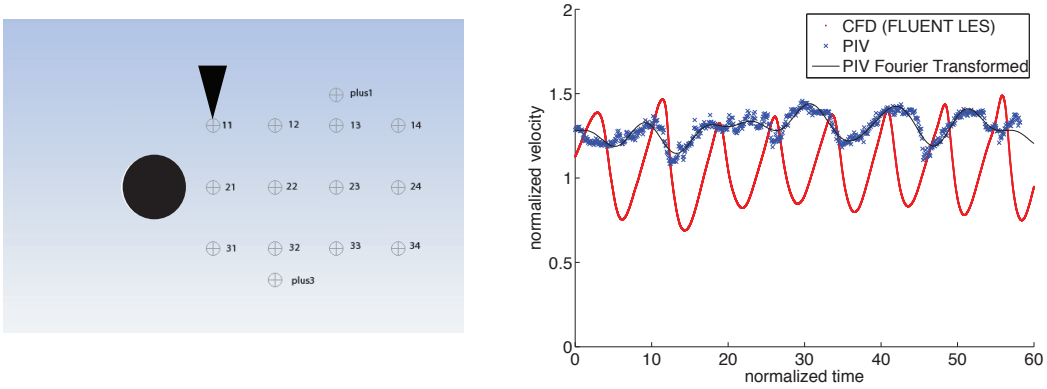


Figure 4.21: Comparison of PIV-measured and LES-predicted horizontal velocities (with cylinder) at point 11

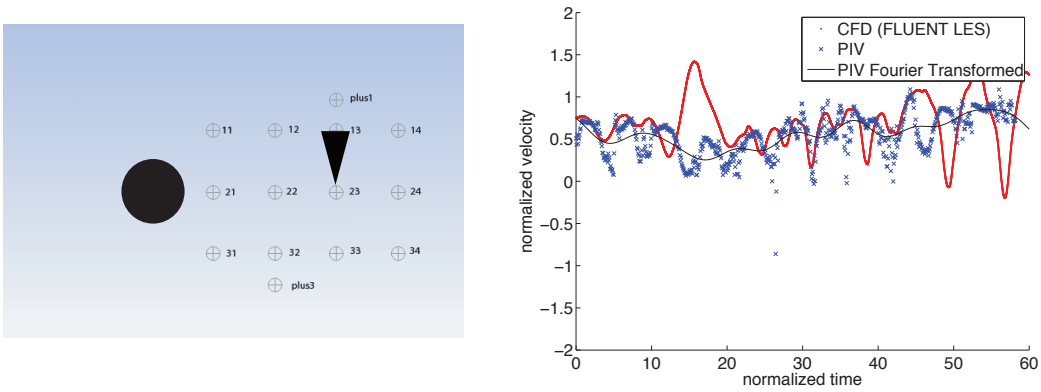


Figure 4.22: Comparison of PIV-measured and LES-predicted horizontal velocities (with cylinder) at point 23

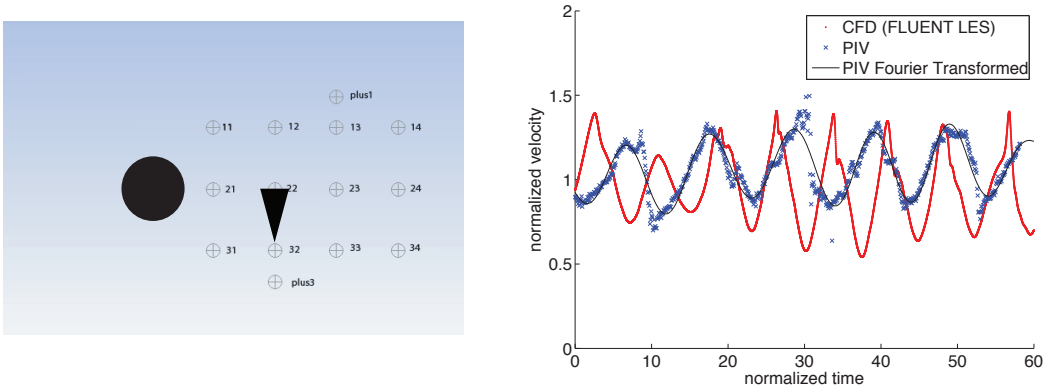


Figure 4.23: Comparison of PIV-measured and LES-predicted horizontal velocities (with cylinder) at point 32

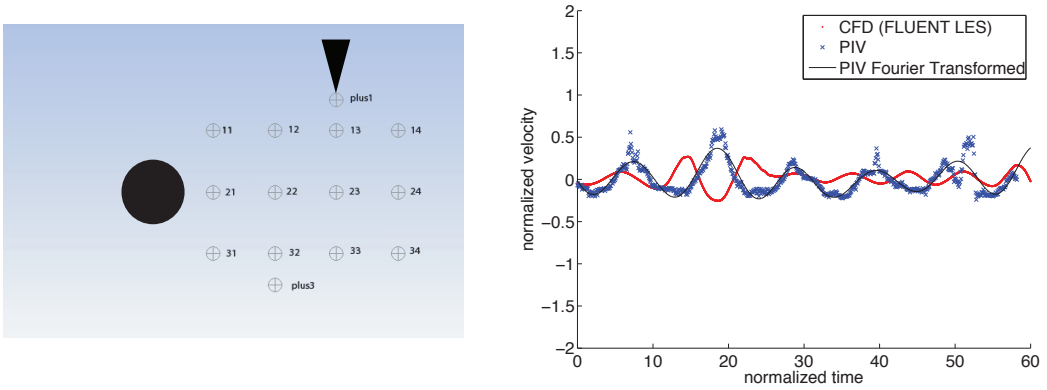


Figure 4.24: Comparison of PIV-measured and LES-predicted vertical velocities (with cylinder) at point PLUS1

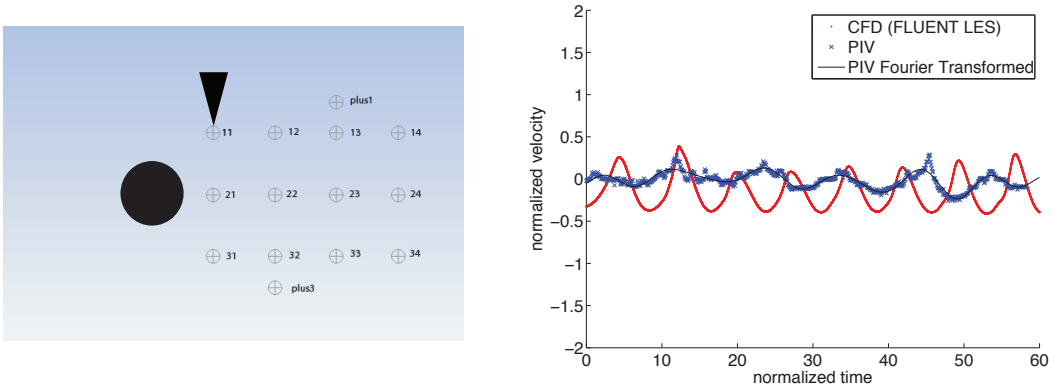


Figure 4.25: Comparison of PIV-measured and LES-predicted vertical velocities (with cylinder) at point 11

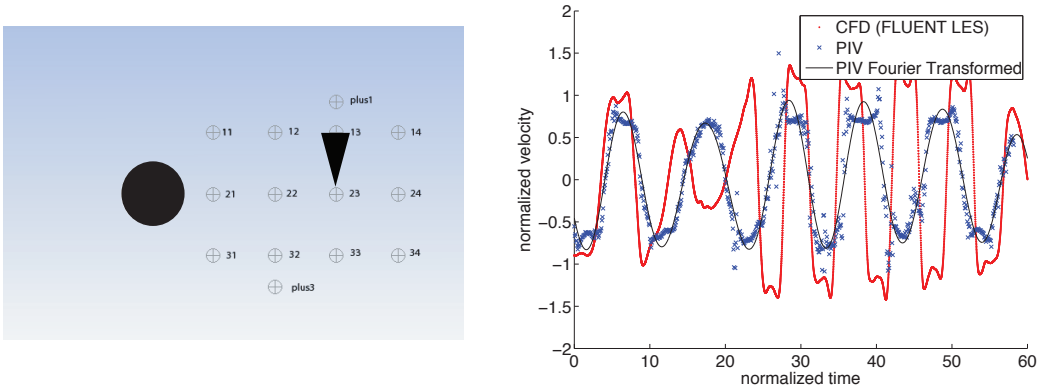


Figure 4.26: Comparison of PIV-measured and LES-predicted vertical velocities (with cylinder) at point 23

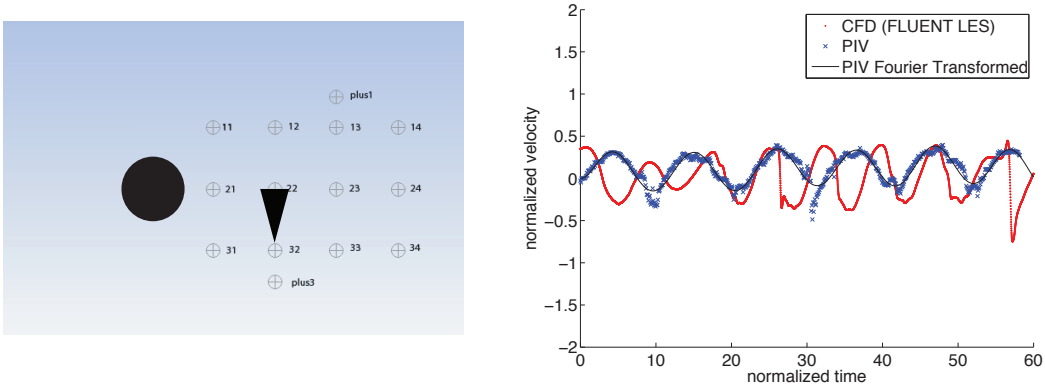


Figure 4.27: Comparison of PIV-measured and LES-predicted vertical velocities (with cylinder) at point 32

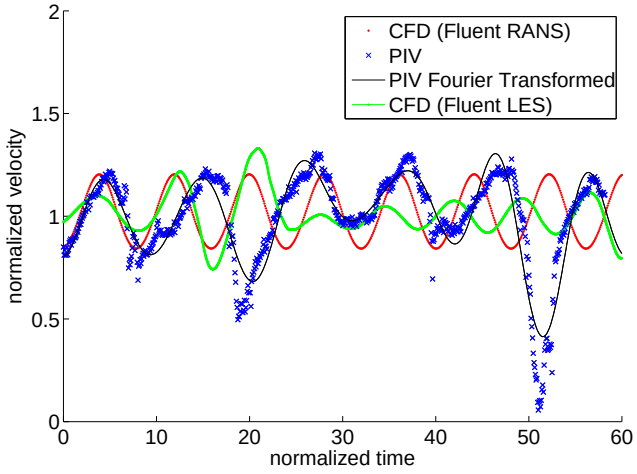


Figure 4.28: Comparison of PIV-measured, RANS-predicted, and LES-predicted horizontal velocities (with cylinder) at point PLUS1

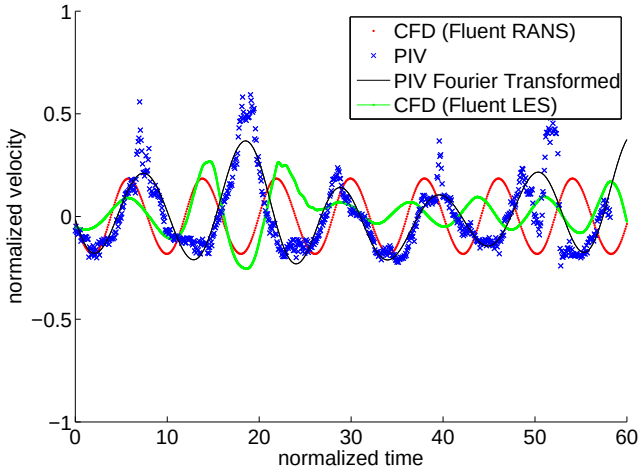


Figure 4.29: Comparison of PIV-measured, RANS-predicted, and LES-predicted horizontal velocities (with cylinder) at point PLUS1

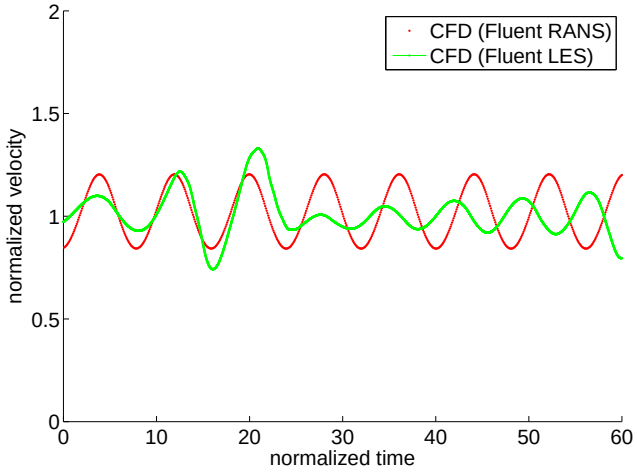


Figure 4.30: Comparison of RANS-predicted and LES-predicted horizontal velocities (with cylinder) at point PLUS1

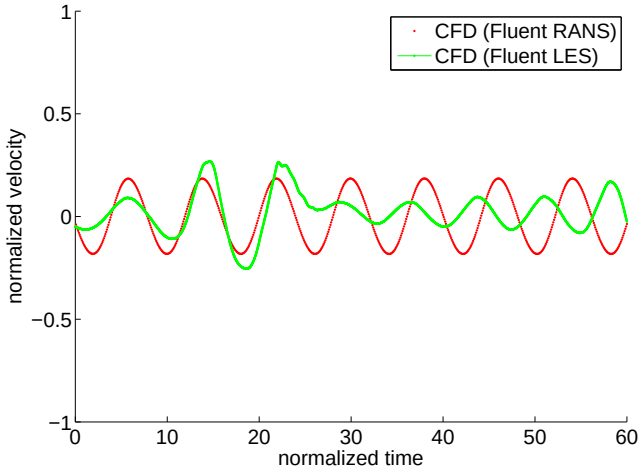


Figure 4.31: Comparison of RANS-predicted and LES-predicted vertical velocities (with cylinder) at point PLUS1

Differences in mean predicted velocities downstream of the cylinder from mean measured velocities (both RANS, Table 4.3, and LES, Table 4.4) are smallest at point PLUS1 and largest at point 11, though point 23 also shows differences of the same order of magnitude. This is true of both horizontal and vertical velocities.

If we assume the PIV values are the "true" values, we can calculate a percent error which ranges between $\approx 1.6\%$ to 73.2% for horizontal velocities in the RANS case and $\approx 1.2\%$ to 67.7% for horizontal velocities in the LES case. The largest percent errors are at point 23 in both the RANS and LES cases (for horizontal velocities). Because the vertical velocities are very small, percent errors quickly become very large and are therefore not discussed.

If we decide that PIV values are not necessarily "true" values due to the intricate process involved in extracting velocity vectors from the PIV images, then we can calculate a percent difference which ranges between $\approx 1.7\%$ to 25.4% for horizontal velocities in the RANS case and $\approx 1.2\%$ to 21.1% for horizontal velocities in the LES case. The largest percent differences are at point 23 in both the RANS and LES cases (for horizontal velocities). The difference in mean velocities predicted between RANS and LES when compared with PIV are relatively minor and it is difficult to say with certainty that one method is more accurate than the other (Tables 4.4 and 4.3).

Given that the velocity predictions from the two-dimensional RANS and LES simulations agree in a general sense with the filtered PIV measurements, the predictions of hydrodynamic coefficients from the RANS and LES

Table 4.3: Difference between mean CFD-predicted (RANS) and PIV-measured (normalized) velocities at several points - cylinder case

| U or V | point | $\tilde{CFD}$ | stdev CFD | $\tilde{PIV}$ | stdev PIV | $\tilde{CFD} - \tilde{PIV}$ |
|---|---|---|---|---|---|---|
| u | plus1 | 1.018 | 0.127 | 1.001 | 0.219 | 0.017 |
| u | 11 | 1.087 | 0.170 | 1.297 | 0.079 | -0.210 |
| u | 23 | 0.721 | 0.090 | 0.559 | 0.240 | 0.163 |
| u | 32 | 0.976 | 0.243 | 1.059 | 0.162 | 0.082 |
| v | plus1 | -0.009 | 0.130 | 0.000 | 0.174 | -0.009 |
| v | 11 | -0.133 | 0.157 | -0.017 | 0.095 | -0.116 |
| v | 23 | -0.048 | 0.871 | -0.013 | 0.605 | -0.035 |
| v | 32 | 0.061 | 0.232 | 0.125 | 0.170 | -0.063 |

are perhaps of use in situations where a general, global average was needed. Such a situation could be the lift and drag coefficients at various locations along a marine riser for use in determining the need for and design specifications for VIV-suppression devices. Since the numerator and denominator of the lift and drag coefficients vary with the square of velocity, we may assume since the CFD-generated velocities were over-predictions of the filtered velocities, the coefficients of drag and lift are also perhaps also over-predicted (Figs. 4.32 and 4.33). The LES-produced average $C_D$ of 1.79 is a bit higher than the RANS-produced average $C_D$ of 1.62 and the frequencies of the signal are almost double the predicted normalized shedding frequency of 0.1, as expected. The frequencies of the LES- and RANS-predicted $C_L$ roughly agree with the theoretical normalized shedding frequency of 0.1. The magnitude of the theoretical $C_D$ for a cylinder in uniform flow at Re=5400 is $\approx 1.2$ [22]. The theoretical $C_D$ for a cylinder in uniform flow is well known which means

Table 4.4: Difference between mean CFD-predicted (LES) and PIV-measured (normalized) velocities at several points - cylinder case

| U or V | point | $\bar{CFD}$ | stdev CFD | $\bar{PIV}$ | stdev PIV | $\bar{CFD} - \bar{PIV}$ |
|---|---|---|---|---|---|---|
| u | plus1 | 1.013 | 0.103 | 1.001 | 0.219 | 0.012 |
| u | 11 | 1.064 | 0.216 | 1.297 | 0.079 | -0.233 |
| u | 23 | 0.691 | 0.298 | 0.559 | 0.240 | 0.132 |
| u | 32 | 0.970 | 0.211 | 1.059 | 0.162 | 0.089 |
| v | plus1 | 0.022 | 0.100 | 0.000 | 0.174 | 0.022 |
| v | 11 | -0.143 | 0.205 | -0.017 | 0.095 | -0.126 |
| v | 23 | -0.009 | 0.883 | -0.013 | 0.605 | -0.004 |
| v | 32 | 0.013 | 0.244 | 0.125 | 0.170 | -0.112 |

that our LES average $C_D$ has a $\approx 49$ % error and our RANS average $C_D$ has a $\approx 35$ % error. Our CFD predictions of $C_D$ are significant overestimates.

## 4.2 Cylinder With Fairing

Because the LES-predicted velocities were not a clear improvement over the RANS-predicted velocities we chose to run the fairing experiments in RANS only. The lack of increased accuracy relative to the very large additional computational cost of LES was a factor in this decision.

The RANS-predicted velocities around the fairing are compared to raw and fit PIV velocities (horizontal: Figs. 4.34, 4.35, 4.36 and 4.37); (vertical: Figs. 4.38, 4.39, 4.40 and 4.41). While horizontal velocities at point 11 (Fig. 4.35) appear to behave well, this point is located in an area outside of the wake. Point PLUS1 is in the wake of the PIV flow while not in the CFD flow and the discrepancy is apparent (Fig. 4.34). The points in the 3rd row (e.g.

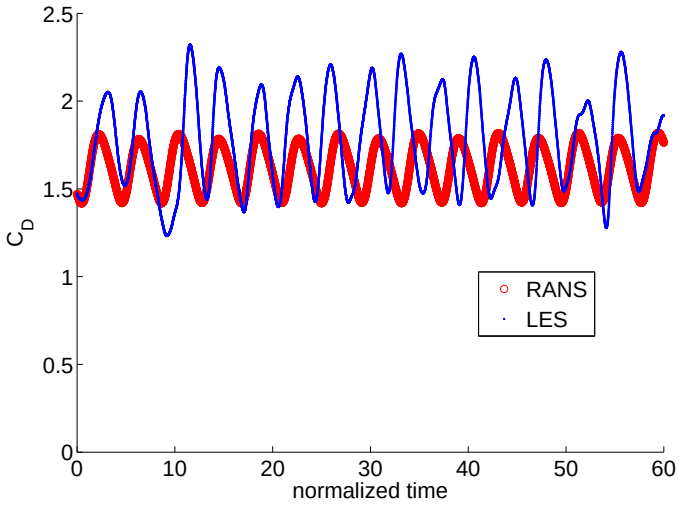


Figure 4.32: Comparison of RANS- and LES-predicted $C_D$ for cylinder

Fig. 4.37) are in a zone of active shedding in the PIV flow while not so in the CFD flow. These discrepancies highlight how much accuracy is lost in the zone of active shedding, downstream of the bluff body, and how much the turbulence is damped in RANS relative to the PIV flow.

The vertical velocities appear to be much better predicted in terms of amplitude when compared to the horizontal predicted velocities. In the immediate lee of the fairing (e.g. Fig. 4.40) we see the amplitude is somewhat over-predicted.

Despite over-predictions, mean velocities are still relatively similar between CFD-predicted and PIV-measured data in the fairing case (Table 4.5) but slightly less so than in the cylinder-only case (Table 4.3). Percent errors range from $\approx$ 13.9% to 181.3% and percent differences range from $\approx$ 2.8%

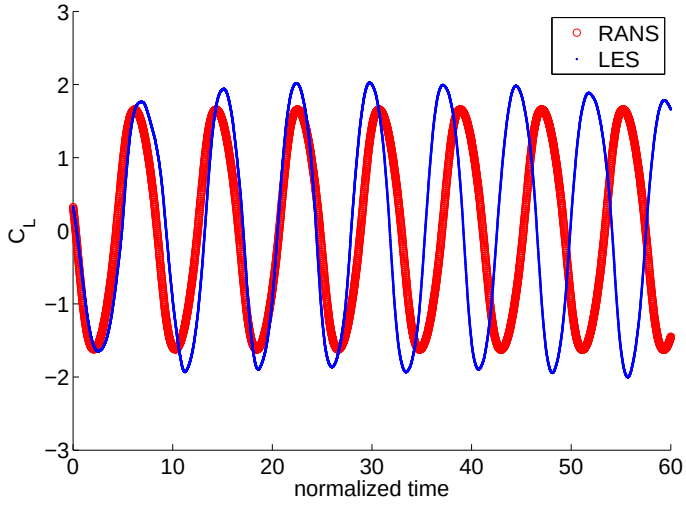


Figure 4.33: Comparison of RANS- and LES-predicted $C_L$ for cylinder

to 629.63% (note: the very large percent errors result from very small mean velocities).

Drag and lift predictions are shown for the fairing relative to the cylinder (RANS-predicted) in figures 4.42 and 4.43. If we assume that PIV and CFD agree enough to make basic statements about hydrodynamic coefficients, we can determine from these figures that our fairing design would reduce drag but not lift amplitudes and we should go back to the drawing board for better VIV-suppression before running a more involved model (three-dimensional CFD or towed-tank experiments).

Table 4.5: Difference between mean CFD-predicted (RANS) and PIV-measured (normalized) velocities at several points - fairing case

| U or V | point | $\bar{CFD}$ | stdevCFD | $\bar{PIV}$ | stdevPIV | $\bar{CFD} - \bar{PIV}$ |
|---|---|---|---|---|---|---|
| u | plus1 | 1.065 | 0.087 | 1.313 | 0.076 | -0.248 |
| u | 11 | 1.277 | 0.021 | 1.313 | 0.105 | -0.037 |
| u | 23 | 0.196 | 0.093 | -0.379 | 0.118 | 0.575 |
| u | 32 | 1.281 | 0.081 | 0.544 | 0.390 | 0.738 |
| v | plus1 | -0.100 | 0.087 | 0.000 | 0.080 | -0.100 |
| v | 11 | 0.066 | 0.041 | 0.284 | 0.100 | -0.218 |
| v | 23 | 0.051 | 0.547 | 0.110 | 0.168 | -0.058 |
| v | 32 | 0.197 | 0.073 | 0.002 | 0.234 | 0.195 |

## 4.3 Probable cause for discrepancies between PIV and CFD

In order to explain the discrepancies between some PIV-measured and CFD-predicted velocities at given shared points in the respective domains, it is helpful to look at the vorticities and vector fields relative to the shared points. We will examine the cylinder scenario as the PIV-CFD differences are well represented in this case. Figure 4.44 shows the magnitude vorticity from the RANS run at a time when a positive (counter-clockwise) vortex is being shed. Figure 4.45 shows z-vorticity at a similar point in the shedding cycle. The scales are comparable (after normalization) in shading, but note the CFD figure shows vorticity magnitude. We can see that the vorticities are more coherent structures in the CFD case whereas the vorticities are more disorganized in the PIV case. It is possible this could be measurement or processing error in the experiment, however great care was taken to avoid

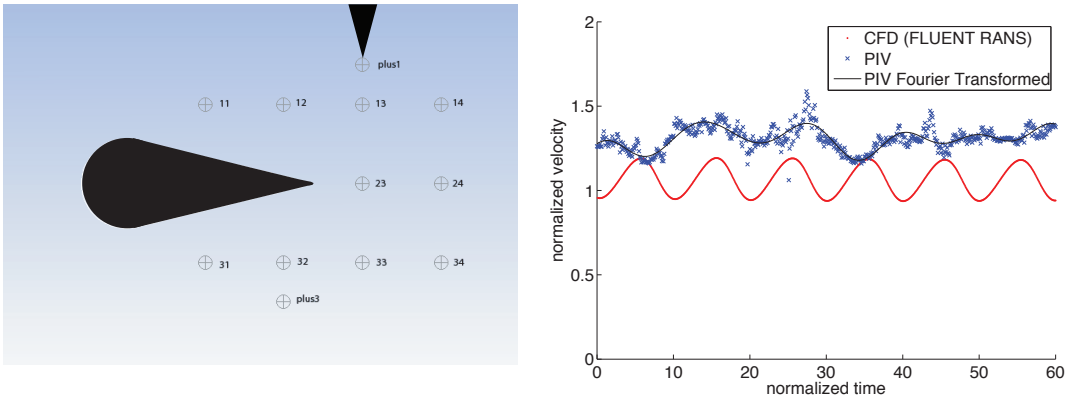


Figure 4.34: Comparison of PIV-measured and RANS-predicted horizontal velocities (with fairing) at point PLUS1

such error.

Additionally, when we compare the CFD generated velocity vectors (Fig. 4.46) to the PIV velocity vectors (Fig. 2.9, we can see that there exists backflow immediately downstream of the cylinder that the CFD doesn't capture. It is near such velocity-tracking points, where the backflow is not captured and the points where turbulent vortices do not reach that the CFD-predicted velocities have the greatest disagreement with PIV-measured velocities. For example, take the horizontal velocity comparison at point PLUS1 (Fig. 4.12). At this point, generally the CFD-predictions accurately match the PIV-measurements, except where occasional turbulent vortices pass through the point. These vortices do not shed far above the cylinder in CFD, but as evidenced by the PIV measurements, this is a limitation of the CFD model used.

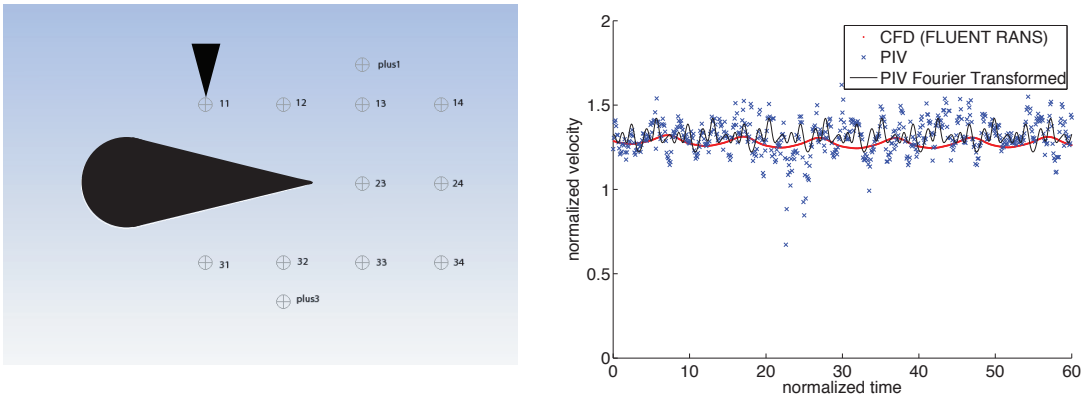


Figure 4.35: Comparison of PIV-measured and RANS-predicted horizontal velocities (with fairing) at point 11

In the case of the fairing, CFD-predictions also appear to miss backflow in the lee of the bluff body. This is especially clear in figure 4.36 where CFD horizontal velocities are positive and PIV horizontal velocities are negative. It is also worth noting that the disagreement at point PLUS1 (Fig. 4.34) is likely due to the wake from the PIV case (Fig. 2.15) not being accurately captured by CFD (Figs. 4.47 and 4.48).

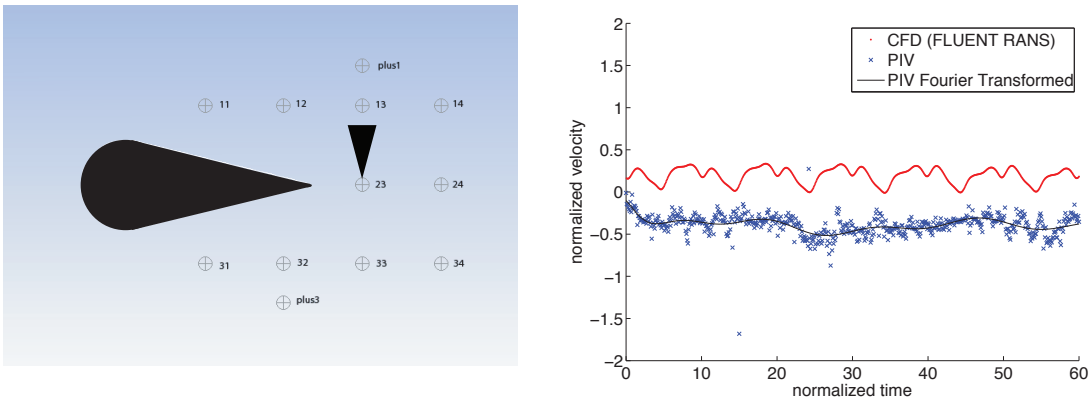


Figure 4.36: Comparison of PIV-measured and RANS-predicted horizontal velocities (with fairing) at point 23

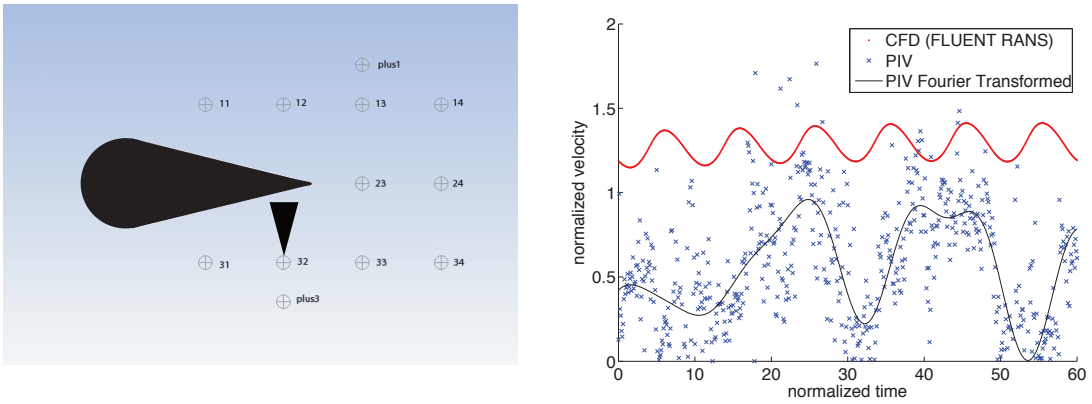


Figure 4.37: Comparison of PIV-measured and RANS-predicted horizontal velocities (with fairing) at point 32

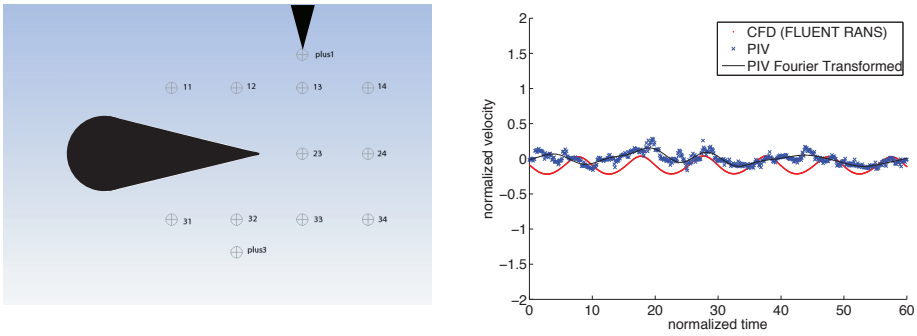


Figure 4.38: Comparison of PIV-measured and RANS-predicted vertical velocities (with fairing) at point PLUS1

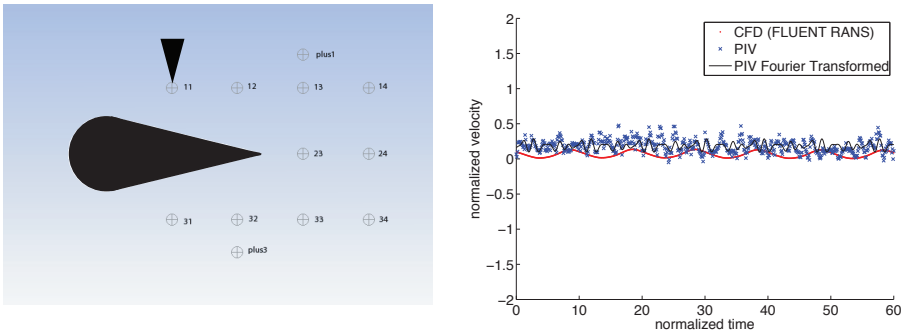


Figure 4.39: Comparison of PIV-measured and RANS-predicted vertical velocities (with fairing) at point 11

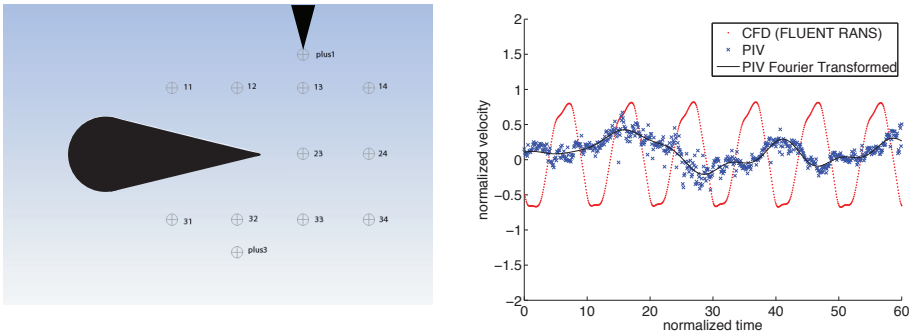


Figure 4.40: Comparison of PIV-measured and RANS-predicted vertical velocities (with fairing) at point 23

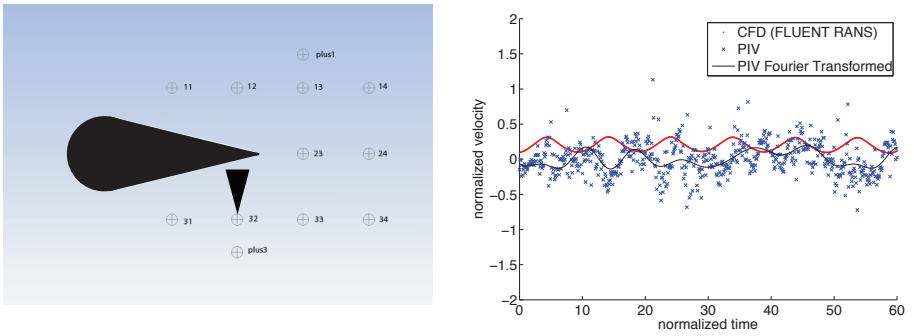


Figure 4.41: Comparison of PIV-measured and RANS-predicted vertical velocities (with fairing) at point 32

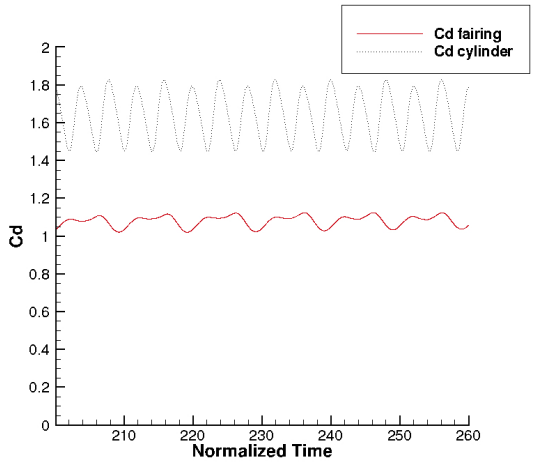


Figure 4.42: Comparison of drag coefficents for cylinder and fairing (RANS predicted)

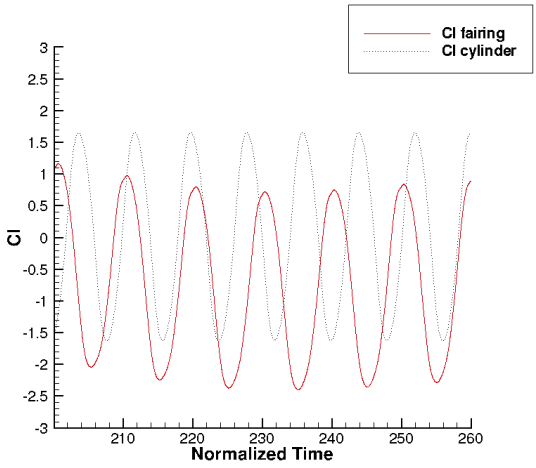


Figure 4.43: Comparison of lift coefficents for cylinder and fairing (RANS predicted)

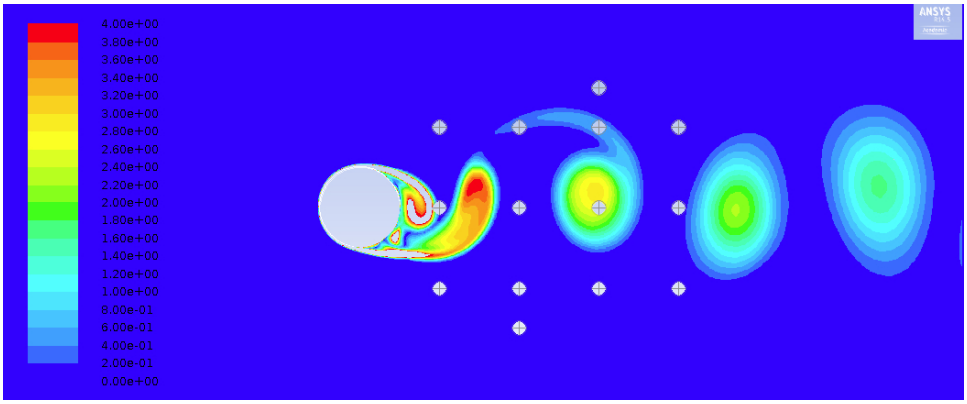


Figure 4.44: Snapshot of vorticity magnitude (1/s′) from RANS cylinder case when positive vortex is shed. Velocity comparison points marked for reference

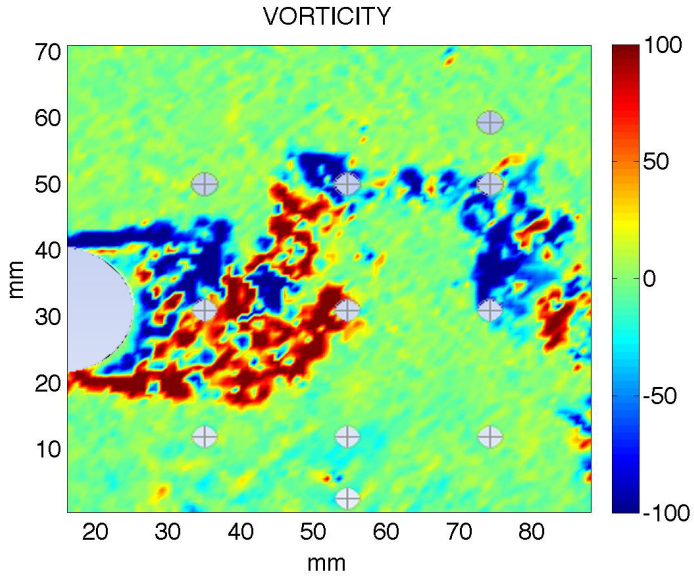


Figure 4.45: Snapshot of Z-Vorticity (1/s) from PIV-measured data when positive vortex is shed. Velocity comparison points marked for reference

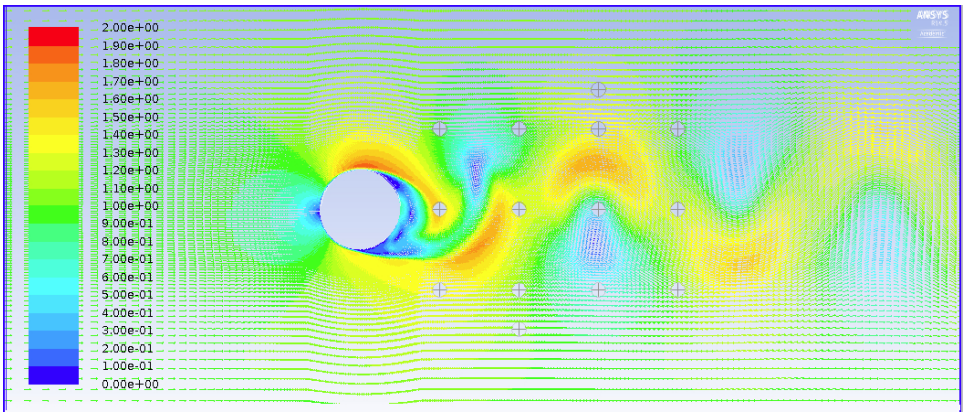


Figure 4.46: Snapshot of normalized velocity vectors (colored by magnitude) as a positive vortex is shed (predicted by RANS). Velocity comparison points marked for reference

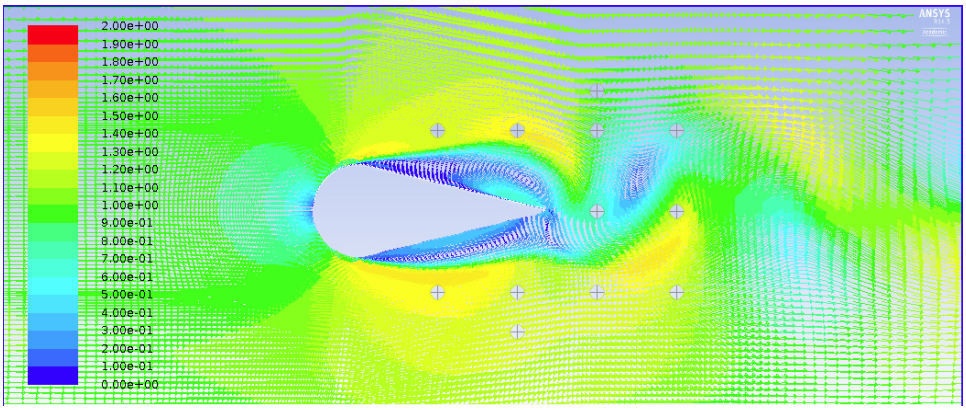


Figure 4.47: Snapshot of normalized velocity vectors (colored by magnitude) as a positive vortex is shed from fairing (predicted by RANS). Velocity comparison points marked for reference

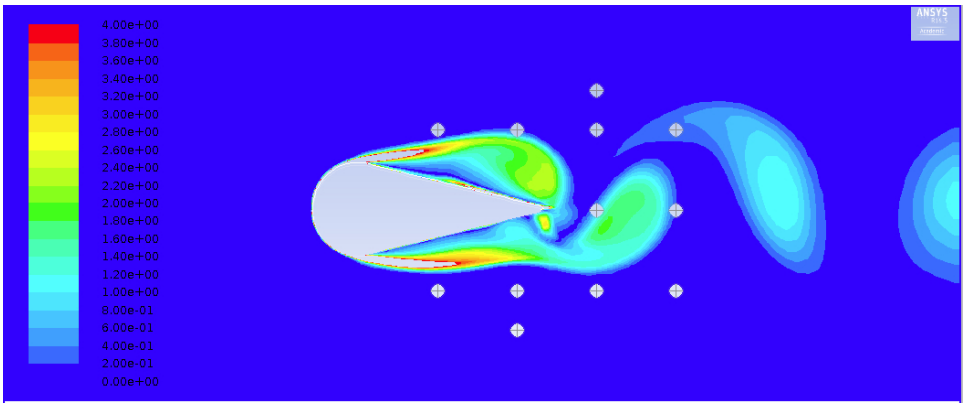


Figure 4.48: Snapshot of normalized vorticity magnitude (predicted by RANS) as a positive vortex is shed. Velocity comparison points marked for reference

# Chapter 5

# Conclusions and Recommendations for Future Work

Accurately predicting flow around a cylinder in two-dimensions is not a trivial task, nor is measuring and interpreting the flow via PIV. The PIV experimental data suggest that a two-dimensional slice can represent the flow in a general sense, but the picture is incomplete. As discussed earlier, the three-dimensionality of turbulence makes modeling turbulence in two-dimensions difficult. A two-dimensional CFD model of the flow, however, is much less expensive (computationally and time-wise) than a three-dimensional simulation. With the vector field comparison, we established that in a general sense a two-dimensional model can capture the basic physics of the flow (i.e. vortex shedding occurs in both at reasonably similar time scales and magnitudes). With the velocity point comparison we examined the accuracy and shortcomings of a two-dimensional model of a three-dimensional phenomenon. Therefore, if only general agreement is required, as perhaps would be appropriate for the beginning stages of design, two-dimensional CFD can be a sufficient starting place. Given that the RANS results were equally reliable (in an average sense) as LES when compared to the filtered PIV measurements, and given that RANS is more robust and less computationally expensive than LES

(as also previously noted by others, [25]), we suggest that RANS is the appropriate tool for a relatively"cheap and quick" approximation of the flow. While LES has been offered as the optimal alternative to DNS, this is perhaps more true in the case of fully three-dimensional simulations. It is important to note, however, that the time averaging that occurs in RANS smoothes the data. With LES this was less so, and turbulent excursions from an average periodic flow were better captured (at a large computational cost).

While we used commercial packages to compare CFD predictions to the PIV data, we hope that our PIV results will be of use to those developing their own RANS and LES codes. The direct comparison between the two-dimensional CFD and two-dimensional PIV presented here should further such goals by showing where the methods disagree (closer the the immediate lee of the cylinder and fairing) and agree (further from the immediate downstream of the cylinder and fairing).

Future work involves replicating in CFD the PIV experiments in three dimensions to quantify the degree to which the three-dimensionality of the turbulence affects predictions of the flow, and incorporating force measurements in the flume experiment for direct $C_D$ and $C_L$ comparisons. Even though extra care was taken to resolve laminar sublayers in calculations, more systematic studies into the effect of grid resolution in the wake (including adaptive gridding) on velocity and vorticity predictions would be beneficial. Additionally, another fairing design with a less blunt head would be worth investigating to see if reduced lift can be attained in CFD, relative to the lift on the cylinder.

# Bibliography

[1] H. Al-Jamal and C. Dalton. Vortex induced vibrations using large eddy simulations at a moderate Reynolds number. *Journal of Fluids and Structures*, 19:73–92, 2004.

[2] D.W. Allen and C. Wayne Allen. Fairings versus helical strakes for suppression of vortex-induced vibration: Installation, maintenance, and economic comparisons. Offshore Technology Conference, Houston TX, USA, 2008. OTC 19374.

[3] D.W. Allen and D.L. Henning. Comparisons of various fairing geometries for vortex suppression at high Reynolds numbers. Offshore Technology Conference, Houston TX, USA, 2008. OTC 19377.

[4] D.W. Allen, L. Lee, and D.L. Henning. Fairings versus helical strakes for suppression of vortex-induced vibration: Technical comparisons. Offshore Technology Conference, Houston TX, USA, 2008. OTC 19373.

[5] S.P. Armstrong. Application of CFD for vortex-induced vibration analysis of marine risers in projects. Offshore Technology Conference, Houston TX, USA, 2008. OTC 18362.

[6] G.R.S. Assi, P.W. Bearman, and N. Kitney. Low drag solutions for suppressing vortex-induced vibrations of circular cylinders. *Journal of*

*Fluids and Structures*, 25:666–675, 2009.

[7] E.R. Balch, W.K. Kavanagh, P.E. Griffen, and L.E. Chouinard. Running fairings for deepwater drilling in the Gulf of Mexico - A cost-benefit approach to deciding the faired length. Offshore Technology Conference, Houston TX, USA, 2003. OTC 15286.

[8] H.M. Blackburn, R.N. Govardhan, and C.H.K. Williamson. A complimentary numerical and physical investigation of vortex-induced vibration. *Journal of Fluids and Structures*, 15:481–488, 2000.

[9] Robert D. Blevins. *Flow-Induced Vibration.* Kreiger Publishing Company, Malabar, Florida, 2001.

[10] M. Bruer. A challenging test case for large eddy simulation: High Reynolds number circular cylinder flow. *International Journal of Heat and FLuid Flow*, 21:648–654, 2000.

[11] J.R. Chaplin, P.W. Bearman, Y. Cheng, E. Fontaine, J.M.R Graham, K. Herfjord, F.J. Huera Huarte, M. Isherwood, K. Lambrakos, C.M Larsen, J.R. Meneghini, G. Moe, R.J. Pattenden, M.S. Triantafyllou, and R.H.J. Willden. Blind predictions of laboratory measurements of vortex-induced vibrations of a tension riser. *Journal of Fluids and Structures*, 21:25–40, 2005.

[12] J.R. Chaplin, P.W. Bearman, F.J. Huera Huarte, and R.J. Pattenden. Laboratory measurements of vortex-induced vibrations of a vertical ten-

sion riser in a stepped current. *Journal of Fluids and Structures*, 21:2–24, 2005.

[13] Dantec Dynamics. *2D PIV Reference Manual*. Dantec Dynamics, Skovlunde, Denmark, latest edition.

[14] M. Dixon and D. Charlesworth. Application of cfd for vortex-induced vibration analysis of marine risers in projects. Offshore Technology Conference, Houston TX, USA, 2006. OTC 18348.

[15] S. Dong and G.E. Karniadakis. DNS of flow past a stationary and oscillating cylinder at Re=10,000. *Journal of Fluids and Structures*, 20:519–531, 2005.

[16] R. Galvao, E. Lee, D. Farrell, F. Hover, M. Triantafyllou, and N. Kitney. Flow control in flow-structure interaction. *Journal of Fluids and Structures*, 24:1216–1226, 2008.

[17] G. Grimminger. The effect of rigid guide vanes on the vibration and drag of a towed circular cylinder. David Taylor Model Basin Report 504, United States Navy, 1945.

[18] L. Han, X. Yu, and S.A. Kinnas. Experimental and numerical studies on unsteady flow around a circular cylinder subjected to waves. Proceedings of the Twenty-second International Offshore and Polar Engineering Conference, Rhodes, Greece, 2012.

[19] K. Huang, H. Chen, and C. Chen. Riser VIV analysis by a CFD approach. Proceedings of the Seventeenth International Offshore and Polar Engineering Conference, Lisbon, Portugal, 2003.

[20] N. Jauvtis and C.H.K. Williamson. The effect of two degrees of freedom on vortex-induced vibration at low mass and damping. *Journal of Fluid Mechanics*, 509:23–62, 2004.

[21] A. Khalak and C.H.K. Williamson. Motions, forces, and mode transitions in vortex-induced vibrations at low mass-damping. *Journal of Fluids and Structures*, 13:813–851, 1999.

[22] B.L. Miller, J.F. Mayberry, and I.J. Salter. The drag of roughened cylinders at high Reynolds numbers. *NPL Rept. Division of Marine Science*, April 1975.

[23] A. Pinto, R. Broglia, A. Di Mascio, E.F. Campana, and P. Rocco. Numerical investigation of the unsteady flow at high Reynolds number over a marine riser with helical strakes. Proceedings of the 25th International Conference on Offshore Mechanics and Arctic Engineering, Hamburg, Germany, 2006.

[24] A. Roshko. On the wake and drag of bluff bodies. *Journal of Aeronautical Science*, 22:124–135, 1955.

[25] T. Sarpkaya. A critical review of the intrinsic nature of vortex-induced vibration. *Journal of Fluids and Structures*, 19:389–477, 2004.

[26] M. Shur, P.R. Spalart, K.D. Squires, M. Strelets, and A. Travin. Three dimesnionality in reyonlds-averaged navier-stokes solutions around two-dimensional geometries. *AIAA Journal*, 43(6):1230–1242, June 2005.

[27] K. Skaugset and R. Baarholm. Effect of marine growth on an elastically mounted circular cylinder. Proceedings OMAE, Estoril, Portugal, 2008. OMAE2008-57586.

[28] M.A. Tognarelli, M. Campbell, and D. Deka. Drilling riser viv - fact or fiction? IADC/SPE Drilling Conference and Exibition, New Orleans, USA, 2010. IADC/SPE 129125.

[29] A.D. Trim, H. Braaten, H. Lie, and M.A. Tognarelli. Experimental investigation of vortex-induced vibration of long marine risers. *Journal of Fluids and Structures*, 21:335–361, 2005.

[30] J.K. Vandiver. *Shear7 Program Use Manual*. MIT, Cambridge, MA, 1999.

[31] B.J Vickery and R.D. Watkins. Flow-induced vibrations fo cylindrical structures. Proceedings of the First Australian Conference on Hydraulics and Fluid Mechanics, Australia, 1964.

[32] C.H.K. Williamson and R. Govardhan. Vortex-induced vibrations. *Annual Review of Fluid Mechanics*, 36:413–455, 2004.

[33] M.M. Zdravkovich. Review and classification of various aerodynamic and hydrodynamic means for suppressing vortex shedding. *Journal of Wind Engineering and Industrial Aerodynamics*, 7:141–189, 1981.